Biophysical Journal Volume 74 March 1998 1149–1168

Cardiac Ca^{2+} Dynamics: The Roles of Ryanodine Receptor Adaptation and Sarcoplasmic Reticulum Load

M. Saleet Jafri, J. Jeremy Rice, and Raimond L. Winslow

Department of Biomedical Engineering, The Johns Hopkins University School of Medicine, Baltimore, Maryland 21205 USA

ABSTRACT We construct a detailed mathematical model for Ca^{2+} regulation in the ventricular myocyte that includes novel descriptions of subcellular mechanisms based on recent experimental findings: 1) the Keizer-Levine model for the ryanodine receptor (RyR), which displays adaptation at elevated Ca^{2+}; 2) a model for the L-type Ca^{2+} channel that inactivates by mode switching; and 3) a restricted subspace into which the RyRs and L-type Ca^{2+} channels empty and interact via Ca^{2+}. We add membrane currents from the Luo-Rudy Phase II ventricular cell model to our description of Ca^{2+} handling to formulate a new model for ventricular action potentials and Ca^{2+} regulation. The model can simulate Ca^{2+} transients during an action potential similar to those seen experimentally. The subspace $[Ca^{2+}]$ rises more rapidly and reaches a higher level (10–30 μM) than the bulk myoplasmic Ca^{2+} (peak $[Ca^{2+}]_i \approx 1$ μM). Termination of sarcoplasmic reticulum (SR) Ca^{2+} release is predominately due to emptying of the SR, but is influenced by RyR adaptation. Because force generation is roughly proportional to peak myoplasmic Ca^{2+}, we use $[Ca^{2+}]_i$ in the model to explore the effects of pacing rate on force generation. The model reproduces transitions seen in force generation due to changes in pacing that cannot be simulated by previous models. Simulation of such complex phenomena requires an interplay of both RyR adaptation and the degree of SR Ca^{2+} loading. This model, therefore, shows improved behavior over existing models that lack detailed descriptions of subcellular Ca^{2+} regulatory mechanisms.

INTRODUCTION

There are several models for cardiac action potentials (APs) that include intracellular Ca^{2+} handling (DiFrancesco and Noble, 1985; Luo and Rudy, 1994a, b; Nordin, 1993; Lindblad et al., 1996). The two most well known are the Luo-Rudy Phase II ventricular cell model and the DiFrancesco-Noble Purkinje cell model. Whereas these models generate APs using biophysically detailed descriptions of membrane currents, the calcium subsystem is represented by a phenomenological model that mimics Ca^{2+}-induced Ca^{2+} release (CICR), but fails to capture the biophysical detail of the mechanisms involved. Other models exist that describe only the Ca^{2+} handling aspects of the cardiac myocyte (Dupont et al., 1996; Tang and Othmer, 1994; Schouten et al., 1987). However, these models do not include the membrane currents, and thus, cannot capture the interplay between the Ca^{2+} subsystems and membrane currents. Such shortcomings have limited the predictive ability of the models with regard to Ca^{2+} dynamics and force generation.

New experimental evidence concerning the RyR and L-type Ca^{2+} current now provides a basis for biophysical models of Ca^{2+} handling in cardiac cells, and for the integration of these models into existing descriptions of the cardiac AP. Recently, Györke and Fill (1993) used lipid bilayer preparations to show that the RyR displays "adaptation" in response to successive Ca^{2+} elevations. Adaptation means that incremental release of Ca^{2+} from RyR occurs in response to incremental step changes in cytoplasmic side Ca^{2+}. Mechanisms of adaptation have been postulated and presented in mathematical models by several groups (Keizer and Levine, 1996; Sachs et al., 1995; Cheng et al., 1995; Tang and Othmer, 1994).

Clearly, properties of CICR and adaptation of RyR will have an important influence on the detailed shape of the cardiac cell Ca^{2+} transient. The shape of this Ca^{2+} transient is also influenced by properties of Ca^{2+}-mediated inactivation of the L-type Ca^{2+} channel (Grantham and Cannell, 1996). Recently, Imredy and Yue (1994) have provided direct evidence concerning the molecular mechanism of this inactivation. Specifically, they have proposed that as Ca^{2+} binds to the L-type Ca^{2+} channel, the channel undergoes a mode switch from one characterized by dense bouts of activity (mode normal) to one typified by infrequent openings (mode Ca). This results in time-dependent inactivation kinetics that are very different from those seen in previous cardiac Ca^{2+} channel models (DiFrancesco and Noble, 1985; Luo and Rudy, 1994a, b; Nordin, 1993).

In this paper we formulate a multimodal model of Ca^{2+}-mediated inactivation of the L-type Ca^{2+} channel based on the concept of mode switching. We incorporate this model, along with a modified version of the Keizer-Levine RyR adaptation model and membrane currents from the Luo-Rudy Phase II model, into a model for ventricular cell Ca^{2+} handling. We then use the model to explore the effects of RyR adaptation and SR load on the cardiac action potential. We also investigate the interplay of RyR adaptation and SR load on the frequency-dependent aspects of the cardiac Ca^{2+} transient.

Received for publication 24 April 1997 and in final form 14 November 1997.

Address reprint requests to Dr. M. Saleet Jafri, Department of Biomedical Engineering, The Johns Hopkins University School of Medicine, Room 411, Taylor Research Building, 720 Rutland Ave., Baltimore, MD 21205. Tel.: 410-502-5091; Fax: 410-614-0166; E-mail: jafri@bme.jhu.edu.

0006-3495/98/03/1149/20 $2.00

MECHANISMS

Our model is based on the Luo-Rudy Phase II model for ventricular action potentials with several modifications (Fig. 1): 1) the Luo-Rudy Phase II L-type Ca^{2+} current is replaced with our new formulation based on the mode-switching behavior observed in rats by Imredy and Yue (1994); 2) the Luo-Rudy Phase II Ca^{2+} SR release mechanism is replaced with the Keizer-Levine RyR model with adaptation (Keizer and Levine, 1996) based on data from isolated canine RyRs; 3) the RyRs and L-type Ca^{2+} channels are assumed to empty into a restricted subspace located between the junctional sarcoplasmic reticulum (JSR) and T-tubules; 4) both high- and low-affinity Ca^{2+} binding sites for troponin are included; 5) the magnitude of the Luo-Rudy Phase II membrane currents I_{K_p}, I_{Na}, I_{NaCa}, $I_{ns(Ca)}$, and $I_{Ca,b}$ are scaled to preserve myoplasmic ionic concentrations and AP shape. Table 6 (Appendix 3) shows the parameters for the membrane currents. Those that were rescaled have their original Luo-Rudy Phase II values shown in parentheses.

L-type Ca^{2+} channel

Ca^{2+}-mediated inactivation of the L-type channels has been shown recently to result from an intrinsic channel Ca^{2+}-binding motif called an EF-hand (de Leon et al., 1995). The discovery of this Ca^{2+}-binding site is important because it suggests that inactivation depends on local Ca^{2+} concentration instead of other hypothesized extrinsic mechanisms such as phosphorylation or second messengers. Inactivation occurs as Ca^{2+} binding induces the channel to switch (from mode normal) to a mode in which transitions to open states are extremely slow (mode Ca), as described in a model by Imredy and Yue (1994). It should be noted that this method of inactivation differs from that of current cardiac cell models. In these models, inactivation is a saturating Michaelis-Menten-type function of $[Ca^{2+}]_i$ that can instantaneously prevent channel permeation. In contrast, the model of Imredy and Yue predicts that inactivation via mode switching occurs with some delay after channel activation. Similarly, the model predicts that recovery to mode normal is not instantaneous when Ca^{2+} concentration falls.

The data of Imredy and Yue show that with an increase of local Ca^{2+}, the L-type channel shifts to a gating mode that shows very infrequent openings. The original Imredy-Yue model described this two-mode behavior with five states (three in mode normal and two in mode Ca), and serves as the starting point of an improved L-type channel model described here. To complete the original Imredy-Yue channel model, the following features are added: 1) additional states; 2) improved Ca^{2+} inactivation, 3) voltage-dependent activation; 4) voltage-dependent inactivation; and 5) open-channel ion permeation.

A state diagram for mode switching and voltage-dependent activation is shown in Fig. 2. The upper and lower rows of states comprise the mode normal and mode Ca, respectively. The channel is assumed to be composed of four independent subunits that can each close the channel. This dictates five closed states (C_0–C_4) on the top row and a mirror set of closed states (C_{Ca0}–C_{Ca4}) on the bottom row. The proportionality of the forward or reverse rates between the closed states is dictated by the four-way symmetry assumed for the channel subunits. Voltage-dependent activation is incorporated through α and β, which are increasing and decreasing functions of voltage. When in the rightmost closed states, C_4 or C_{Ca4}, there are voltage-independent transitions to the open states, O or O_{Ca}. Note that f' is 500 times slower than f, so that openings are rare in mode Ca, effectively inactivating the channel.

The transitions to mode Ca are controlled by γ, which is a function of Ca^{2+}. As one moves right in Fig. 2, there are

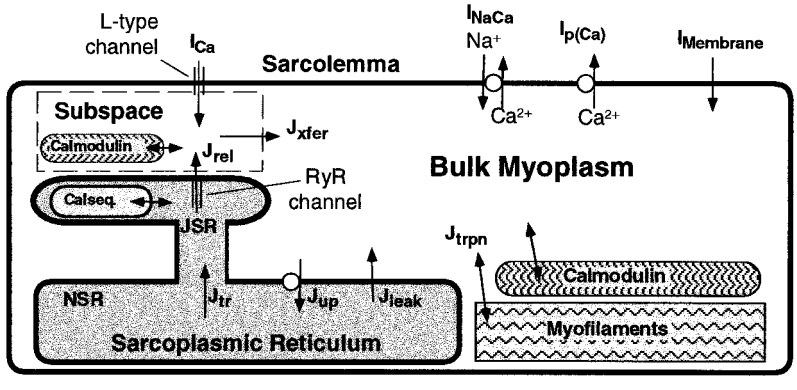

FIGURE 1 Schematic diagram of mechanisms involved in cardiac Ca^{2+} dynamics. In response to membrane depolarization during an AP, L-type Ca^{2+} channels open, allowing the influx of Ca^{2+} (I_{Ca}) into a restricted subspace, where it triggers Ca^{2+} release from the JSR (J_{rel}) via ryanodine receptors (RyR). Ca^{2+} diffuses from the subspace to the bulk myoplasm (J_{xfer}), where it is removed from the cell by Na^+-Ca^{2+} exchangers (I_{NaCa}) and ATP-dependent Ca^{2+} pumps ($I_{p(Ca)}$) or resequestered into NSR by SERCA pumps (J_{up}). The JSR is refilled by diffusion from the NSR (J_{tr}). Ca^{2+} is buffered by calmodulin in the subspace and myoplasm, by troponin in the myoplasm, and by calsequestrin in the JSR. There is a leak (J_{leak}) from the NSR and a background Ca^{2+} current across the sarcolemma (included in $I_{membrane}$), which help to maintain Ca^{2+} homeostasis. $I_{membrane}$ includes all of the other transarcolemmal currents that are not defined above.

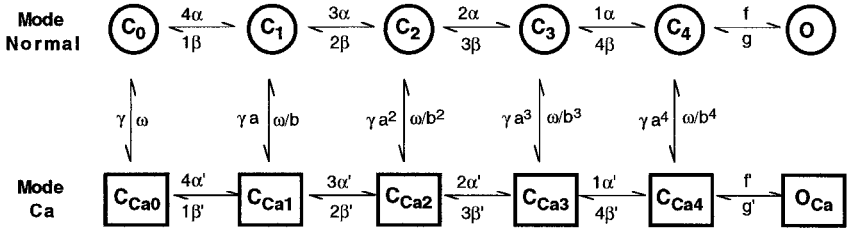

FIGURE 2 Schematic diagram for the transitions between the states of the L-type Ca^{2+} channel. The upper row of states comprises the mode normal, and the lower row comprises mode Ca. The channel is composed of four independent subunits, each of which can close the channel. The corresponding states are C_n, where n is the number of permissive subunits. With depolarization, the channels undergo transitions from left to right. With four permissive subunits, there is a voltage-independent transition to the conducting state O. With elevation of $[Ca^{2+}]_{ss}$ the channel transition occurs from the mode normal (*top*) to mode Ca (*bottom*). $f' \ll f$, so that transitions into O_{Ca} are rare, which effectively inactivates the channel in mode Ca.

incremental increases in the multiplier of γ and the divisor on ω. The effect of this is to greatly increase the transition rate to mode Ca at high voltages when the channel is opening. The close symmetry between mode normal and mode Ca closed states and similarity of rates (i.e., g versus g') is dictated by the experimental finding that gating currents are very similar in the mode normal and mode Ca cases (Shirokov et al., 1993; Hadley and Lederer, 1991). Additional constraints on the rate constants come from thermodynamic microreversibility. Microreversibility requires that for each cycle, the product of rates is equal whether taken in the clockwise or the counterclockwise direction. A similar formulation and state diagram has been proposed for N-type Ca^{2+} channels in bullfrog sympathetic neuron (Cory et al., 1993).

Voltage-dependent inactivation is modeled as a Hodgkin-Huxley-type gate. This gate can inactivate the channel independently of the states already discussed above. The time constant of inactivation is significantly longer than that of existing models of L-type current (DiFrancesco and Noble, 1985; Luo and Rudy, 1994a). These previous models probably underestimated the time constant of voltage-dependent inactivation, because the temporal properties of Ca^{2+}-induced inactivation were not appropriately considered. That is, Ca^{2+}-induced inactivation was assumed to be an instantaneous function of $[Ca^{2+}]_i$ with dynamics due solely to voltage-gated inactivation.

L-type channels have complex permeation properties, showing extremely high selectivity coupled with high open channel flux rates (Hess, 1990; Hille, 1992). To account for these properties, researchers have proposed a number of multiple binding site models (Hess and Tsien, 1984). However, these permeation models were not chosen for the improved Ca^{2+} subsystem because 1) their relatively high complexity would substantially increase computation and data storage demand; and 2) none of the models are consistent with all of the experimental data (Hess, 1990). A much simpler approach, used in existing cardiac models (Luo and Rudy, 1994a; DiFrancesco and Noble, 1985; Nordin and Ming, 1995), makes use of a Goldman-Hodgkin-Katz (GHK) formalism with large permeability for Ca^{2+} coupled to smaller permeabilities for K^+ and Na^+. However, this approach is also unsatisfactory because 1) the open channel current-voltage (I-V) relations do not match experimental results; and 2) GHK assumes that ionic species permeate independently (Hille, 1992), whereas data indicate essentially no monovalent permeation while the channel is passing significant amounts of Ca^{2+} current. As a compromise between the complex multisite models and the simpler GHK formalism, a novel permeation model is employed. In this model, it is assumed that 1) the Ca^{2+} current follows constant field theory and is the only inward current passing through the channel; and b) the permeability of K^+ is a decreasing function of Ca^{2+} current. Under these assumptions, it becomes increasingly hard for K^+ to pass when the channel is occupied by Ca^{2+} ions. The $P_{K'}$ (the permeability of K^+ as modified by the Ca^{2+} current I_{Ca}) is given by

$$P_{K'} = \frac{\bar{P}_K}{1 + \dfrac{I_{Ca}}{I_{Ca_{half}}}}, \tag{1}$$

where $\bar{P}_K$ is the permeability of K^+ in the absence of Ca^{2+} current, I_{Ca} is L-type Ca^{2+} current, and $I_{Ca_{half}}$ is the level of Ca^{2+} current that reduces the permeability of K^+ by 50%.

Open-channel I-V relations for this permeation model are shown by the solid trace in Fig. 3 *A*. The dashed traces show the separate contributions from the Ca^{2+} and K^+ currents. In Fig. 3 *B*, the open-channel I-V relation is multiplied by the open probability (ignoring voltage and Ca^{2+}-induced inactivation) to effectively simulate voltage clamp data, where peak current is measured before the channel inactivates significantly. The model data are similar to experimentally determined I-V relations (McDonald et al., 1986).

Ryanodine receptors

Ca^{2+} release from the JSR is based on a model for RyR by Keizer and Levine (Fig. 4). This model has two open states (P_{O_1} and P_{O_2}) and two closed states (P_{C_1} and P_{C_2}). At rest, the channel resides primarily in the first closed state, P_{C_1}. Upon an increase in Ca^{2+}, the channel switches briefly to the first open state P_{O_1}, allowing Ca^{2+} to move through the

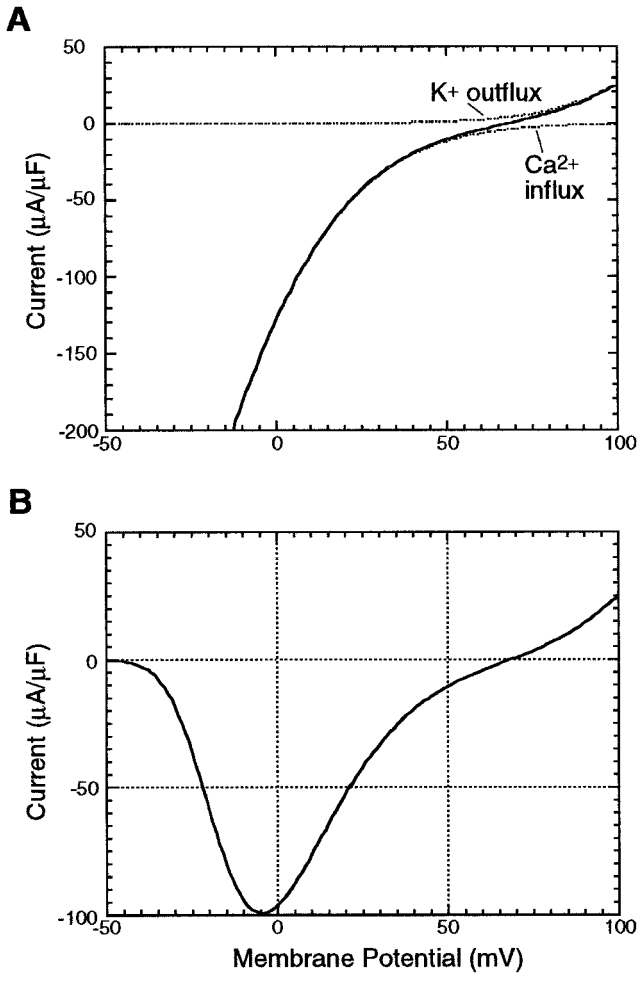

FIGURE 3 (*A*) Open L-type Ca^{2+} channel *I-V* relation for the permeation model (*solid line*), and the separate contributions by Ca^{2+} influx and K^+ efflux (*dashed lines*). (*B*) Peak I_{Ca} obtained by multiplying the open channel *I-V* relation from above with the maximum open channel probability.

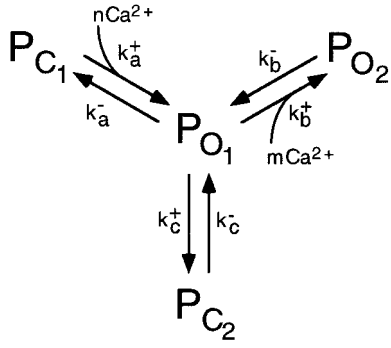

FIGURE 4 Schematic diagram of the transitions between the states of the RyR. P_{C_1} and P_{C_2} are closed states, and P_{0_1} and P_{0_2} are open states. The k's are the transition rates. The transitions from P_{C_1} to P_{0_1} and from P_{0_1} to P_{0_2} are Ca^{2+} dependent. At resting Ca^{2+} levels, most of the channels are in state P_{C_1}. With an increase in Ca^{2+}, the channels undergo transitions to P_{0_1} before channel adaptation by transition to P_{C_2}. Additional increases in Ca^{2+} cause reopening by transitions into P_{0_2}.

channel, before it adapts by its transition to P_{C_2}. Upon additional increases in Ca^{2+}, the channel reopens by its transition to state P_{O_2}, displaying the adaptive behavior seen experimentally (Györke and Fill, 1993). More recent experimental evidence (Valdivia et al., 1995) suggests that in the presence of physiological levels of cytosolic Mg^{2+}, the rate of adaptation is faster than the findings of the original experiments by Györke and Fill, which lacked Mg^{2+}. We follow the suggestion of Keizer and Levine that a faster rate for k_c^+ would account for this finding. The bilayer experiments by Györke and Fill were performed at room temperature (25°C), whereas our model describes a cardiac ventricular cell at 37°C. To account for this difference, all of the rate constants are increased over the original Keizer and Levine values.

The RyR is also modified to account for the environment of the subspace. The Keizer-Levine model assumes that the RyR can be exposed to peak $[Ca^{2+}]_i$ (Appendix 2) values of ~1.0 μM. In our model, the RyR is located in the subspace, where it is exposed to $[Ca^{2+}]_{ss}$ in excess of 10.0 μM (Santana et al., 1996; Cannell et al., 1994; Isenberg, 1995). In addition, $[Ca^{2+}]_{ss}$ levels change more rapidly than $[Ca^{2+}]_i$. Thus the rate constants are modified to adjust the channel sensitivity to Ca^{2+}, so that the channel functions properly in the appropriate Ca^{2+} range (Table 3, Appendix 3.3).

Subspace

Many existing cardiac AP models have Ca^{2+} influx from an L-type channel and release from SR via RyR emptying into the bulk myoplasm (DiFrancesco and Noble, 1985; Luo and Rudy, 1994a, b). In contrast, many researchers have suggested that both of these channels empty into a more restricted subspace, where Ca^{2+} concentration may increase to much greater levels than in the bulk myoplasm (Isenberg, 1995; Nordin, 1993; Stern, 1992; Bers, 1991; Lederer et al., 1990). The anatomical evidence suggests that L-type and RyR channels exist in a ratio of 1:5.6 in the guinea pig (Bers and Stiffel, 1992). The channels are located in specialized junctional areas, where T-tubular membrane and SR membrane are separated by a junctional gap of 12 nm (Frank, 1990). Following Isenberg (1995), we define a functional unit as four L-type channels surrounded by 25 RyRs. Assuming that the RyRs are arranged in 5 × 5 array according to a spacing of 60 nm, the cluster will cover a surface area of 300 nm × 300 nm. The number of functional units can be estimated as 5500 L-type channels per cell (Isenberg, 1995) divided by four channels per functional unit. The volume of the restricted subspace can be estimated by

$$V_{ss} = (\text{junctional gap}) \times (\text{area of functional unit}) \times (\text{number of functional units}). \quad (2)$$

The volume of the subspace is then calculated as 1.485×10^{-9} μl. For comparison, this volume is about four orders

of magnitude smaller than the total volume of the myoplasm (25.84×10^{-6} μl).

The rate of Ca^{2+} flux out of this subspace (J_{xfer}) allows $[Ca^{2+}]_{ss}$ and $[Ca^{2+}]_i$ to equilibrate with a time constant τ_{xfer} (Eq. 8).

Buffering

Ca^{2+} buffers sequester in excess of 98% of the total Ca^{2+} released during a contraction (Berlin et al., 1994). These buffers are distributed between mobile and stationary buffers. In cardiac cells, the mobile buffer is calmodulin, and the stationary buffers are troponin and myosin (Robertson et al., 1981). In previous models, the effects of myosin have been ignored because, in simulations by Robertson and co-workers, it was never more than 2.3% saturated during a Ca^{2+} transient (Robertson et al., 1981). Calsequestrin is the most abundant SR luminal Ca^{2+}-binding protein (Isenberg, 1995). Immunoelectron microscopy has shown that calsequestrin is located in the JSR and not in the NSR (Jorgensen and Campbell, 1984).

Buffers B bind Ca^{2+} by the following equation:

$$B + Ca^{2+} \rightleftharpoons BCa^{2+}. \tag{3}$$

If the kinetics of binding is fast compared to Ca^{2+} release, Eq. 3 remains close to equilibrium during the Ca^{2+} transient. In this case, the rapid buffering approximation is used (Wagner and Keizer, 1994). Calsequestrin and calmodulin are considered to be fast buffers, based on their rate constants (Robertson et al., 1981; Cannell and Allen, 1984). Otherwise, Ca^{2+} binding to buffers lags behind the equilibrium values, as is the case with troponin. In this case, differential equations based on reaction kinetics must be solved. Both the high- and low-affinity sites for troponin are used in this model.

MODEL EQUATIONS

Ca^{2+} subsystem

The Ca^{2+} subsystem consists of 10 differential equations specifying the time rate of change in 1) the myoplasmic Ca^{2+} concentration ($[Ca^{2+}]_i$); 2) the subspace Ca^{2+} concentration ($[Ca^{2+}]_{ss}$); 3) the junctional SR Ca^{2+} concentration ($[Ca^{2+}]_{JSR}$); 4) the network SR Ca^{2+} concentration ($[Ca^{2+}]_{NSR}$); 5) the probability that RyR is in the first closed state (P_{C_1}); 6) the probability that RyR is in the first open state (P_{O_1}); 7) the probability that RyR is in the second open state (P_{O_2}); 8) the probability that RyR is in the second closed state (P_{C_2}); 9) the concentration of Ca^{2+} bound to high-affinity troponin-binding sites ([HTRPNCa]); and 10) the concentration of Ca^{2+} bound to low-affinity troponin-binding sites ([LTRPNCa]). The other buffers, calsequestrin in the JSR, and calmodulin in the myoplasm and subspace ($[CSQN]_{JSR}$, $[CMDN]_i$, and $[CMDN]_{ss}$, respectively), are fast buffers, so the rapid buffering approximation is used to minimize computation (Wagner and Keizer, 1994).

There are six Ca^{2+} fluxes to consider in the subsystem: 1) the Ca^{2+}-induced Ca^{2+} release (CICR) flux via the RyR (J_{rel}; Eq. 4); 2) the leak flux from the NSR to the myoplasm (J_{leak}; Eq. 5); 3) the Ca^{2+} uptake flux by the SR Ca^{2+}-ATPase pump (J_{up}; Eq. 6); 4) the transfer flux of Ca^{2+} from the NSR to the JSR (J_{tr}; Eq. 7); 5) the transfer flux from the subspace to the myoplasm (J_{xfer}; Eq. 8); and 6) the buffering flux of Ca^{2+} binding to troponin (J_{trpn}; Eq. 9). Three additional membrane current fluxes are necessary for the formulation of Ca^{2+} regulation: 7) the pump current ($I_{p(Ca)}$; Eq. 84) flux of Ca^{2+} removal from the cell; 8) the L-type Ca^{2+} channel Ca^{2+} flux (I_{Ca}; Eq. 37); and 9) the Na^+-Ca^{2+} exchange current (I_{NaCa}; Eq. 75) Ca^{2+} flux.

The RyR channel flux is described by

$$J_{rel} = v_1(RyR_{open})([Ca^{2+}]_{JSR} - [Ca^{2+}]_{ss}), \tag{4}$$

where v_1 is the maximum RyR channel Ca^{2+} flux, and RyR_{open} is the sum of the fraction of channels in the RyR channel open states P_{O_1} and P_{O_2} ($RyR_{open} = P_{O_1} + P_{O_2}$). The equations describing RyR are given in Appendix 2. The leak from the NSR into the myoplasm is given by

$$J_{leak} = v_2([Ca^{2+}]_{NSR} - [Ca^{2+}]_i), \tag{5}$$

where v_2 is the Ca^{2+} leak rate constant from the NSR. Ca^{2+} uptake into the NSR by the SR Ca^{2+}-ATPase pump is given by

$$J_{up} = v_3 \frac{[Ca^{2+}]_i^2}{K_{m,up}^2 + [Ca^{2+}]_i^2}, \tag{6}$$

where v_3 is the SR Ca^{2+}-ATPase (SERCA2a) maximum pump rate, and $K_{m,up}$ is the half-saturation constant for the SR Ca^{2+}-ATPase pumps. In this model, the SR Ca^{2+}-ATPase pump has a Hill coefficient of 2, consistent with recent experimental findings (Lytton et al., 1992). The transfer flux of Ca^{2+} from the JSR to the NSR is described by

$$J_{tr} = \frac{[Ca^{2+}]_{NSR} - [Ca^{2+}]_{JSR}}{\tau_{tr}}, \tag{7}$$

where τ_{tr} is the time constant for transfer from NSR to JSR. The transfer flux from the subspace to the myoplasm is

$$J_{xfer} = \frac{[Ca^{2+}]_{ss} - [Ca^{2+}]_i}{\tau_{xfer}}, \tag{8}$$

where τ_{xfer} is the time constant for transfer from subspace to myoplasm. Buffering by troponin is described by

$$\begin{aligned} J_{trpn} = {} & k_{htrpn}^{+}[Ca^{2+}]_i([HTRPN]_{tot} - [HTRPNCa]) \\ & - k_{htrpn}^{-}[HTRPNCa] \\ & + k_{ltrpn}^{+}[Ca^{2+}]_i([LTRPN]_{tot} - [LTRPNCa]) \\ & - k_{ltrpn}^{-}[LTRPNCa], \end{aligned} \tag{9}$$

where $[LTRPN]_{tot}$ is the total myoplasmic troponin low-affinity site concentration, $[HTRPN]_{tot}$ is the total myoplas-

mic troponin high-affinity site concentration, k^{+}_{htrpn} is the Ca^{2+} on rate constant for troponin high-affinity sites, k^{-}_{htrpn} is the Ca^{2+} off rate constant for troponin high-affinity sites, k^{+}_{ltrpn} is the Ca^{2+} on rate constant for troponin low-affinity sites, and k^{-}_{ltrpn} is the Ca^{2+} on rate constant for troponin low-affinity sites. The first term in Eq. 9 describes the rate of Ca^{2+} binding to troponin high-affinity Ca^{2+}-binding sites. The second term describes the off rate from these sites. The third and fourth terms (second line) describe the on and off rates for Ca^{2+} binding to troponin low-affinity binding sites, respectively.

The buffering effects of calmodulin and calsequestrin can be approximated by the rapid buffering approximation (Wagner and Keizer, 1994). This simplification assumes that the free and bound Ca^{2+} buffers with fast kinetics are at equilibrium. Using this assumption, a Ca^{2+}-dependent function can be found that will scale the fluxes that comprise the time rate of change in total free Ca^{2+} by the factors B_i, B_{ss}, and B_{JSR} for the myoplasm, subspace, and JSR, respectively:

$$B_i = \left\{1 + \frac{[CMDN]_{tot} K_m^{CMDN}}{(K_m^{CMDN} + [Ca^{2+}]_i)^2}\right\}^{-1}, \tag{10}$$

$$B_{ss} = \left\{1 + \frac{[CMDN]_{tot} K_m^{CMDN}}{(K_m^{CMDN} + [Ca^{2+}]_{ss})^2}\right\}^{-1}, \tag{11}$$

$$B_{JSR} = \left\{1 + \frac{[CSQN]_{tot} K_m^{CSQN}}{(K_m^{CSQN} + [Ca^{2+}]_{JSR})^2}\right\}^{-1}. \tag{12}$$

The balance equation for $[Ca^{2+}]_i$ is

$$\frac{d[Ca^{2+}]_i}{dt} = B_i\left\{J_{leak} + J_{xfer} - J_{up} - J_{trpn} + (I_{Ca,b} - 2I_{NaCa} + I_{p(Ca)})\frac{A_{cap}}{2V_{myo}F}\right\}, \tag{13}$$

where A_{cap} is the capacitive membrane area, V_{myo} is the myoplasmic volume, 2 is the valence of Ca^{2+}, and F is Faraday's constant. Changes to $[Ca^{2+}]_{ss}$ are determined by

$$\frac{d[Ca^{2+}]_{ss}}{dt} = B_{ss}\left\{J_{rel}\frac{V_{JSR}}{V_{ss}} - J_{xfer}\frac{V_{myo}}{V_{ss}} + (I_{Ca})\frac{A_{cap}}{2V_{ss}F}\right\}. \tag{14}$$

Note that the fluxes J_{rel} and J_{xfer} are scaled for the volume of the compartment. A detailed description of L-type Ca^{2+} current is presented in the next section. The $[Ca^{2+}]_{JSR}$ and $[Ca^{2+}]_{NSR}$ balance equations are

$$\frac{d[Ca^{2+}]_{JSR}}{dt} = B_{JSR}\{J_{tr} - J_{rel}\}, \tag{15}$$

$$\frac{d[Ca^{2+}]_{NSR}}{dt} = \{J_{up} - J_{leak}\}\frac{V_{myo}}{V_{NSR}} + J_{tr}\frac{V_{JSR}}{V_{NSR}}. \tag{16}$$

L-type Ca^{2+} channel

We created a new mathematical model to describe the L-type channel that is based on the experimentally observed mode-switching behavior of the channel. The rate constants for the L-type Ca^{2+} channel depend on the parameters in Table 4 (Appendix 3) and

$$\alpha = 0.4e^{(V+12)/10} \tag{17}$$

$$\beta = 0.05e^{(V+12)/13} \tag{18}$$

$$\alpha' = \alpha a \tag{19}$$

$$\beta' = \frac{\beta}{b} \tag{20}$$

$$\gamma = 0.1875[Ca^{2+}]_{ss}, \tag{21}$$

where α, β, γ, α', and β' are in units of ms^{-1}. This yields the following set of equations for channel states:

$$\frac{dC_0}{dt} = \beta C_1 + \omega C_{Ca0} - (4\alpha + \gamma)C_0 \tag{22}$$

$$\frac{dC_1}{dt} = 4\alpha C_0 + 2\beta C_2 + \frac{\omega}{b}C_{Ca1} - (\beta + 3\alpha + \gamma a)C_1 \tag{23}$$

$$\frac{dC_2}{dt} = 3\alpha C_1 + 3\beta C_3 + \frac{\omega}{b^2}C_{Ca2} - (2\beta + 2\alpha + \gamma a^2)C_2 \tag{24}$$

$$\frac{dC_3}{dt} = 2\alpha C_2 + 4\beta C_4 + \frac{\omega}{b^3}C_{Ca3} - (3\beta + \alpha + \gamma a^3)C_3 \tag{25}$$

$$\frac{dC_4}{dt} = \alpha C_3 + gO + \frac{\omega}{b^4}C_{Ca4} - (4\beta + f + \gamma a^4)C_4 \tag{26}$$

$$\frac{dO}{dt} = fC_4 - gO \tag{27}$$

$$\frac{dC_{Ca0}}{dt} = \beta' C_{Ca1} + \gamma C_0 - (4\alpha' + \omega)C_{Ca0} \tag{28}$$

$$\frac{dC_{Ca1}}{dt} = 4\alpha' C_{Ca0} + 2\beta' C_{Ca2} + \gamma a C_1 - \left(\beta' + 3\alpha' + \frac{\omega}{b}\right)C_{Ca1} \tag{29}$$

$$\frac{dC_{Ca2}}{dt} = 3\alpha' C_{Ca1} + 3\beta' C_{Ca3} + \gamma a^2 C_2 - \left(2\beta' + 2\alpha' + \frac{\omega}{b^2}\right)C_{Ca2} \tag{30}$$

$$\frac{dC_{Ca3}}{dt} = 2\alpha' C_{Ca2} + 4\beta' C_{Ca4} + \gamma a^3 C_3 - \left(3\beta' + \alpha' + \frac{\omega}{b^3}\right) C_{Ca3} \quad (31)$$

$$\frac{dC_{Ca4}}{dt} = \alpha' C_{Ca_3} + g' O_{Ca} + \gamma a^4 C_4 - \left(4\beta' + f' + \frac{\omega}{b^4}\right) C_{Ca4} \quad (32)$$

$$\frac{dO_{Ca}}{dt} = f' C_{Ca4} - g' O_{Ca}. \quad (33)$$

The state O in Eq. 27 is the conducting state. Equations 22–27 describe the normal mode, and Eqs. 28–33 describe mode Ca^{2+}. The voltage inactivation gate y of the L-type Ca^{2+} channel is determined by

$$\frac{dy}{dt} = \frac{y_\infty - y}{\tau_y}, \quad (34)$$

where

$$y_\infty = \frac{1}{1 + e^{(V+55)/7.5}} + \frac{0.1}{1 + e^{(-V+21)/6}}, \quad (35)$$

and

$$\tau_y = 20 + \frac{600}{1 + e^{(V+30)/9.5}}. \quad (36)$$

The L-type Ca^{2+} channel can then be written by

$$I_{Ca} = \bar{P}_{Ca} y \{O + O_{Ca}\} 4 \frac{2VF}{RT} \frac{0.001 e^{2VF/RT} - 0.341[Ca]_o}{e^{2VF/RT} - 1}, \quad (37)$$

where $\bar{P}_{Ca}$ is the maximum L-type Ca^{2+} channel conductance, y is the voltage inactivation gate, $\{O + O_{Ca}\}$ is the open probability based on the mode-switching model (Eqs. 27 and 33), and 4 corresponds to the square of the charge of Ca^{2+}. The last expression in Eq. 37 is the electrochemical driving force for L-type Ca^{2+} current. The first term in the numerator of this expression uses 0.001 mM as the product of the activity coefficient of $[Ca^{2+}]_{ss}$ and the concentration at the mouth of the channel. This assumes that once the channel is open, the concentration at the mouth does not change (Smith, 1996). This value was chosen because using the formulation presented by Luo-Rudy failed to give the initial fast rise and peak seen in experimentally measured L-type Ca^{2+} channels.

The final component of the L-type Ca^{2+} channel is the K^+ current through the channel,

$$I_{Ca,K} = P'_K y \{O + O_{Ca}\} \frac{[K^+]_i e^{2VF/RT} - [K^+]_o}{e^{2VF/RT} - 1}. \quad (38)$$

The variables y and $\{O + O_{Ca}\}$ are the same as those described in Eq. 37, and the permeability P'_K is given in Eq. 1. The last term gives the driving force behind $I_{Ca,K}$.

The remaining equations for membrane currents and gating variables are taken from the Luo-Rudy Phase II model and are used to formulate differential equations (Appendix 1). It was necessary to rescale some of these currents: scaling factor of Na^+-Ca^{2+} exchange $k_{NaCa} = 5000$ μA μF^{-1}, maximum Na^+-K^+ exchange current $I_{NaK} = 1.3$ μA μF^{-1}, maximum plateau K^+ channel conductance $\bar{G}_{Kp} = 0.00828$ mS μF^{-1}, maximum Na^+ channel conductance $\bar{G}_{Na} = 12.8$ mS μF^{-1}, maximum background Ca^{2+} current conductance $\bar{G}_{Ca,b} = 0.006032$ mS μF^{-1}, and permeability of nonspecific current channel for K^+ and Na^+ $P_{ns(Ca)} = 0.0$ cms^{-1}. The original Luo-Rudy Phase II values are shown in parentheses in Table 6 (Appendix 3). These mechanisms were rescaled as described above to maintain long-term homeostasis and improve AP shape.

METHODS

The full set of 30 ordinary differential equations was solved on a Silicon Graphics Indy workstation, using the Merson Modified Runge-Kutta 4th-Order Adaptive Step Algorithm (Kubicek and Marek, 1983), with a maximum step size of 0.1 ms and a maximum error tolerance of 10^{-6}. The error from all variables was normalized to ensure that all variables contributed equally to the global error calculation. These variables and their respective weights are V: 100 mV, $[Na^+]_i$: 5 mM, $[K^+]_i$: 140 mM, $[Ca^{2+}]_i$: 0.001 mM, $[Ca^{2+}]_{NSR}$: 2 mM, $[Ca^{2+}]_{ss}$: 0.001 mM, and $[Ca^{2+}]_{JSR}$: 20 mM. All other variables were given weights of 1.0. The results were visualized using Xmgr by Paul J. Turner and PV-WAVE by Precision Visuals.

The standard set of parameters and initial conditions used in the simulations is shown in the tables given in Appendix 3, unless specified in the figure legends or text. Because the original formulation for the Luo-Rudy model is for a ventricular cell of a small mammal like the guinea pig, when possible, the improved Ca^{2+} subsystem is also formulated using experimental data from small mammals. Action potentials were initiated by a 0.1 μA μF^{-1} current injection for 0.5 ms.

RESULTS

Single action potential

The model contains a new formulation for the L-type Ca^{2+} channel. The initial test of the model is to verify that the L-type Ca^{2+} current was consistent in shape and amplitude with experimental values measured by Grantham and Cannell (1996). The model was driven by the AP clamp used by Grantham and Cannell in their study of I_{Ca} (Fig. 5 *A*). Under control conditions and AP clamp, the model generates an I_{Ca} similar to experimentally measured values (Fig. 5 *B*, *solid line*). The contribution of Ca^{2+} inactivation is studied, following the experimental protocol (Grantham and Cannell, 1996) designed to deplete the SR. The external

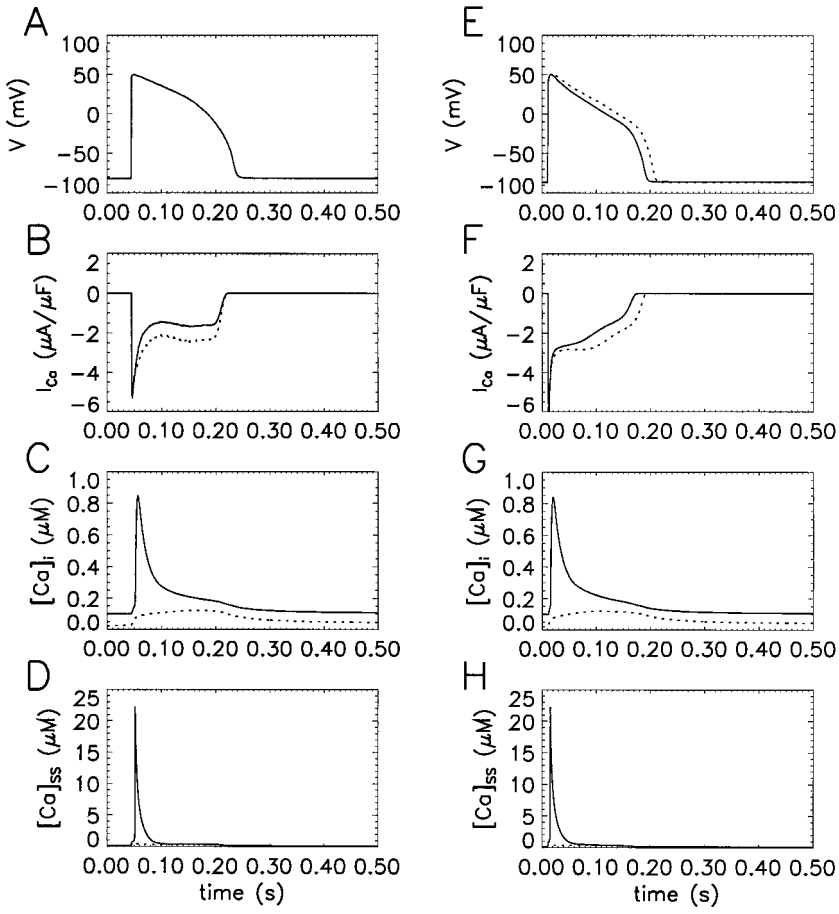

FIGURE 5 Simulations generated by the model in an AP clamp protocol (*A–D*) and in the free-running model (*E–H*). (*A*) Membrane potential trace from the AP clamp used by Grantham and Cannell (1996) to study I_{Ca}. (*B*) I_{Ca} generated by the model during the AP clamp protocol (control, *solid line*; depleted SR, *dotted line*; in all panels). The SR was depleted by pacing for 10 s at 1.0 Hz in low external Ca^{2+} (0.1 mM), with the RyR open fraction set to 0.8 to mimic the effects of caffeine. The external Ca^{2+} was returned to 1.8 mM and the first AP was recorded. (*C*) Myoplasmic Ca^{2+} transient. In the case with depleted SR (*dotted line*), the $[Ca^{2+}]_i$ transient is attenuated. (*D*) The restricted subspace Ca^{2+} transient shows a higher peak and faster dynamics than $[Ca^{2+}]_i$. (*E*) AP generated by the free-running model. The AP with a depleted SR is longer than the control AP. (*F*) I_{Ca} in free-running model. (*G*) Myoplasmic Ca^{2+} transient. (*H*) Subspace Ca^{2+} transient. Parameters and initial conditions are given in the tables in Appendix 3.

Ca^{2+}($[Ca^{2+}]_o$) is reduced to 0.1 mM, and the RyR open fraction (RyR_{open}) is set to 0.8 to mimic the effects of caffeine. The cell is then paced for 10 s at 1.0 Hz (free-running APs). The cell is returned to control conditions: no caffeine ($RyR_{open} = P_{O_1} + P_{O_2}$) and $[Ca^{2+}]_o = 1.8$ mM, and an AP clamp is applied. The I_{Ca} with depleted SR is shown by the dotted line (Fig. 5 *B*). The increase in I_{Ca} is due to the removal of Ca^{2+} inactivation. This is consistent with the findings of Grantham and Cannell (1996). The myoplasmic Ca^{2+} concentration ($[Ca^{2+}]_i$) transient for the control under the AP clamp (Fig. 5 *C*; *solid line*) rises to 0.85 μM from a resting value of 0.10 μM. Under depleted SR conditions, the AP clamp yields a small $[Ca^{2+}]_i$ transient that rises to 0.12 μM from a resting value of 0.02 μM, indicating no Ca^{2+} release from the SR. The subspace Ca^{2+} ($[Ca^{2+}]_{ss}$) in the control simulation under AP clamp (Fig. 5 *D*, *solid line*) rises to a peak of 22.2 μM. With a depleted SR, $[Ca^{2+}]_{ss}$ shows only a relatively small peak of 0.5 μM (Fig. 5 *D*, *dotted line*).

The protocol described above is applied to the free-running model to yield a typical action potential. The initial conditions for this simulation are obtained during diastole from a simulation of a cardiac myocyte paced at 1.0-Hz stimulus frequency. The AP is triggered at 10 ms. The control AP rises to a peak value of 50.4 mV (Fig. 5 *E*, *solid line*). The control AP is shorter in duration and has a lower plateau than the AP with depleted SR (Fig. 5 *E*, *dotted line*). The I_{Ca} generated by the model (Fig. 5 *F*, *solid line*) is similar to those observed in experiments (Grantham and Cannell, 1996) and very close to those observed by Puglisi and Bers (personal communication). The L-type Ca^{2+} current quickly activates, reaching its peak of -6.46 μA μF^{-1} within 2 ms of the stimulus. The initial decrease in the current, giving rise to its spike-like appearance, results from a decline in the L-type Ca^{2+} current as V rises to the peak of the AP. As Fig. 5 *B* shows, at 50 mV the peak L-type Ca^{2+} current through the channel is greatly diminished. A secondary reduction of the current after ~30 ms is produced by Ca^{2+} inactivation. Later in the AP, I_{Ca} is further diminished because of voltage-dependent inactivation (~100 ms). At this time, the high value of $[Ca^{2+}]_{ss}$ drives the channel to mode Ca, which has infrequent openings and hence lowers open probability. With SR depletion, I_{Ca} increases slightly in amplitude and duration (Fig. 5 *F*, *dotted line*) because of the removal of Ca^{2+} inactivation. The longer duration and higher plateau of the SR-depleted AP is due to these changes in I_{Ca}. The $[Ca^{2+}]_i$ transients rises to 0.84 μM from a resting value of 0.10 μM (Fig. 5 *G*, *solid line*). Under depleted SR conditions, the AP yields a small $[Ca^{2+}]_i$ transient that rises to 0.12 μM from a resting value of 0.02

μM, indicating no Ca^{2+} release from the SR (Fig. 5 *G*, *dotted line*).

The Ca^{2+} transient in the control simulation (Fig. 5 *G*, *solid line*) is similar in magnitude and time course to experimental data from the guinea pig (Isenberg, 1995). A typical Ca^{2+} transient measured experimentally reaches a peak of 1.0 μM from a resting value of 0.1 μM. In the model at 1.0 Hz pacing frequency, $[Ca^{2+}]_i$ rises from 0.10 μM during diastole to a peak value of 0.84 μM during an AP, consistent with these estimates of changes in bulk $[Ca^{2+}]_i$. In the guinea pig ventricular myocyte, this Ca^{2+} transient has a duration of ~0.3 s and has a tonic elevation that follows the peak systolic $[Ca^{2+}]_i$ (Isenberg, 1995). The model reproduces this tonic elevation by the shoulder seen in Fig. 5 *G* to the right of the peak. In experiments, Ca^{2+} reaches its peak value (latency) within 20–40 ms and decays within 80–120 ms (Isenberg, 1995). In the model, the latency will not exceed this limit through a wide variety of pulse protocols. For example, in Fig. 5 *G* the latency is 10.0 ms. In contrast, the Ca^{2+} in restricted subspace ($[Ca^{2+}]_{ss}$) cannot yet be quantified experimentally, but is thought to be at least an order of magnitude larger than bulk systolic $[Ca^{2+}]_i$ (Santana et al., 1996). In the model, $[Ca^{2+}]_{ss}$ reaches a peak value of 22.3 μM, as shown in Fig. 5 *H*, starting from a resting value of 0.14 μM. Note that $[Ca^{2+}]_{ss}$ shows a different time course, with much steeper onset and decay, than $[Ca^{2+}]_i$. This demonstrates that $[Ca^{2+}]_{ss}$ and $[Ca^{2+}]_i$ are not just scaled versions of each other, because there is a very different set of sources and sinks for Ca^{2+} in each of the compartments. These will now be examined in more detail.

The intracellular Ca^{2+} fluxes cannot currently be measured, so the following simulation results cannot be compared to experimental data. However, these model results reveal dynamics of the underlying Ca^{2+} subsystem, and predict how these signals might appear in real cells. The RyR flux (J_{rel}) has a peak value ~40 times larger than that of the $J_{I_{Ca}}$, consistent with the large amplification estimated for CICR (Cannell et al., 1994). When total Ca^{2+} influx is summed over the course of the AP, ~10 times more Ca^{2+} enters the subspace from the RyRs than from the L-type channels, consistent with a number of estimates (Isenberg, 1995; Bers, 1991).

Efflux from the subspace is by diffusion to the myoplasm, which is described by the transfer flux out of the subspace (J_{xfer}). The transfer time constant τ_{xfer} is set to a value that is a compromise between two extremes. Small values produce a large concentration peak in the subspace, slow transfer to bulk myoplasm, and possibly restimulate CICR. Large transfer rates cause the influx of trigger Ca^{2+} through the L-type channel to dissipate quickly. This leads to a long latency for the Ca^{2+} transient due to the slowed initiation of CICR. In extreme cases, the rise in concentration of the restricted subspace may be ineffective in producing regenerative CICR.

The major source of influx to the bulk myoplasmic space is from J_{xfer}, the transfer from the subspace to the bulk myoplasm. Another small source of flux into the myoplasm is from the leak of Ca^{2+} out of the SR. The major efflux is the uptake into the SR by the Ca^{2+}-ATPase (J_{up}). A much smaller source of efflux is the Na^+/Ca^{2+} exchanger (I_{NaCa}), but only very late in the AP; this exchanger works in reverse earlier in the AP, producing an influx of Ca^{2+}. I_{NaCa} is electrogenic; in forward mode, three Na^+ ions enter for every Ca^{2+} ion extruded, producing a net inward current. Because of this electrogenic nature, the exchanger shows voltage dependence and works in reverse mode at depolarized potentials. The switch from Na^+ extrusion to Ca^{2+} extrusion occurs later in the AP than in the original Luo-Rudy formulation; however, this late switch from reverse to forward mode is consistent with the I_{NaCa} measured by Grantham and Cannell (1996). The reason for the difference is due to the altered shape of the $[Ca^{2+}]_i$ transient. The Luo-Rudy phase II model has a triangular calcium transient, whereas the Ca^{2+} transients generated by our model more closely simulate experimentally determined Ca^{2+} transients. The smallest source of efflux is the sarcolemmal Ca^{2+} pump. This pump has a high affinity and low throughput, so that it generally contributes little efflux under normal conditions. Its contribution may be important, however, in long-term Ca^{2+} homeostasis or during pathological conditions.

All uptake of Ca^{2+} (J_{up}) is into the network SR (NSR) compartment (Fig. 7 *B*, *dashed line*). There is an initial rise in $[Ca^{2+}]_{NSR}$ resulting from the increase in J_{up} when $[Ca^{2+}]_i$ rises during the AP. All SR release (J_{rel}) comes from the junctional SR (JSR). This release produces the drop in $[Ca^{2+}]_{JSR}$. The depletion of this store is one factor in terminating CICR. Another factor terminating CICR is the decrease in open fraction of the RyRs as a result of adaptation. The JSR store is replenished from a transfer flux from NSR (J_{tr}).

To understand the relative contributions of RyR adaptation and JSR depletion to termination of Ca^{2+} release, we performed simulations that varied either the rate of adaptation or level of JSR Ca^{2+} depletion (Figs. 6 and 7). The first set of simulations studied the contribution of adaption to the termination of Ca^{2+} release from the SR. To eliminate adaptation without perturbing the system too drastically, we set the rate constant k_c^+ for migration into the RyR adapted state C_2 to zero (Fig. 4) and paced the cell at 1.0 Hz until a stable set of APs was reached. When compared to the control simulation ($k_c^+ = 0.018$ ms^{-1}; *solid line*), this results in almost no decrease in AP duration (APD), almost no change in Ca^{2+} release (Fig. 6 *A*, *dotted line*), and a slightly slower time course for $[Ca^{2+}]_{JSR}$ refilling (Fig. 6 *B*, *dotted line*). Fig. 6 *C* (*dotted line*) shows that whereas the opening of the RyR is not significantly delayed, the closing is delayed slightly, resulting in a small increase in the time interval during which RyR open probability is high. The small magnitude of the changes in Fig. 6 show that for the most part, model responses are similar before and after elimination of RyR adaptation.

In the next set of simulations, we examined the effects of increasing the rate of RyR adaptation on Ca^{2+} release. The

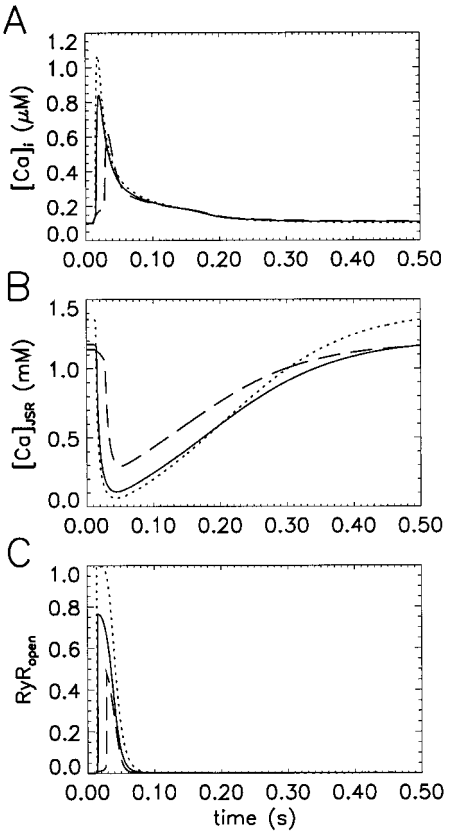

FIGURE 6 The role of RyR adaptation in the termination of Ca^{2+} release during an AP: 1) control simulation with the standard parameter set ($k_c^+ = 0.018\ ms^{-1}$; *solid line*); 2) no adaptation ($k_c^+ = 0.0\ s^{-1}$; *dotted line*); and 3) fast adaptation ($k_c^+ = 0.072\ ms^{-1}$; *dashed line*). The AP with no adaptation is almost indistinguishable from the control. With fast adaptation, the AP has a slightly higher plateau and slightly longer duration. (*A*) The $[Ca^{2+}]_i$ transient with no adaptation is similar to control, whereas with fast adaptation the latency is increased and the amplitude is reduced. (*B*) Depletion of $[Ca^{2+}]_{JSR}$ is delayed and reduced in the case of fast adaptation. In the case of no adaptation, $[Ca^{2+}]_{JSR}$ depletion recovers slightly more slowly than control. (*C*) With no adaptation, the RyR open fraction transient lasts slightly longer than the control. The RyR_{open} transient is smaller, is of shorter duration, and has delayed onset compared to control.

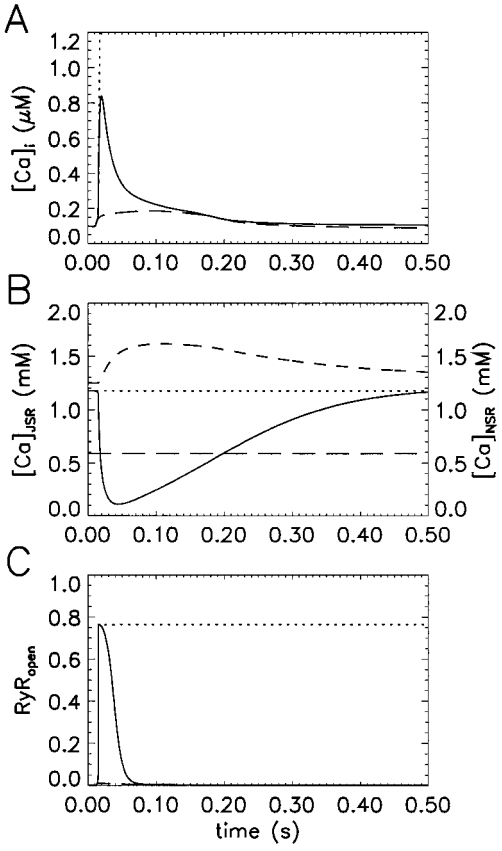

FIGURE 7 The role of SR depletion on the termination of Ca^{2+} release during an AP: 1) control simulation (*solid line*); 2) SR clamp ($[Ca^{2+}]_{JSR} = 1.175$ mM) at resting value ($[Ca^{2+}]_{JSR} = 1.175$ mM; *dotted line*); 3) partial SR clamp at 50% resting value ($[Ca^{2+}]_{JSR} = 0.588$ mM; *long dashed line*). The dashed line shows $[Ca^{2+}]_{NSR}$ in the control simulation. The action potential in the case of SR clamp does not converge, because of never-ending release from the SR (*A*). The partial SR clamp yields an AP with elevated plateau and longer duration. (*A*) The myoplasmic Ca^{2+} transient with SR clamp does not terminate. With the partial SR clamp, there is no Ca^{2+} release from the SR. (*B*) $[Ca^{2+}]_{JSR}$ varies from a resting value of 1.175 mM to a minimum value of 0.108 mM during a control AP. With the SR clamp the value remains fixed at 1.175 mM, whereas during the partial SR clamp the value remains constant at 0.588 mM. (*C*) During SR clamp conditions the RyR open fraction remains at values similar to the peak values during a control. During partial SR clamp, RyR_{open} barely rises at all, indicating minimal release from the SR.

parameter k_c^+ was increased from 0.018 ms^{-1} (Fig. 6, *solid line*) to 0.072 ms^{-1} (Fig. 6, *dotted line*), effectively increasing the rate of adaptation by 4.0 times. Faster rates of adaptation were not used because they resulted in alternans. The model was paced at 1.0 Hz until a stable set of APs was obtained. With the faster adaptation rate, the AP is only slightly longer than the control, with a very slightly elevated plateau (not shown). This lengthening is due to an increase in I_{Ca}, caused by a reduction of Ca^{2+} inactivation in response to the smaller Ca^{2+} transients in the subspace, which results in a small Ca^{2+} transient in the myoplasm. In addition to the smaller magnitude of the $[Ca^{2+}]_i$ transient, the transient also shows a longer latency to peak than control (*solid line*). The longer latency is a result of a lower gain for CICR. This occurs because more of the RyRs are in the adapted state (P_{C_2}), and thus there is a smaller fraction that can quickly make a transition from P_{C_1} to P_{O_1} in response to Ca^{2+} and hence contribute to regenerative release. Depletion of $[Ca^{2+}]_{JSR}$ has a delayed onset and a smaller magnitude than in the control (Fig. 6 *B*). With fast adaptation, the resting $[Ca^{2+}]_{JSR}$ is a little lower than the control levels. The open fraction transient has decreased magnitude and duration (Fig. 6 *C*) compared to control. Hence the simulations suggest that RyR adaptation has a small effect on modulating the Ca^{2+} transient in a single AP.

The next set of simulations shows the effects of SR load on SR release termination. Here $[Ca^{2+}]_{JSR}$ is clamped by reducing its time derivative to zero (SR clamp). With this SR clamp (Fig. 7, *dotted line*), the system becomes unstable and Ca^{2+} release from the SR does not terminate. This is evident in the AP increasing without bound (not shown) due

to increased Na^+-Ca^{2+} exchange, which results from a greatly increased $[Ca^{2+}]_i$ (Fig. 7 *A*). The level of $[Ca^{2+}]_{JSR}$ remains constant at its clamped value of 1.175 mM (Fig. 7 *B*). RyR_{open} for the SR clamp (Fig. 7 *C*, *dotted line*) rises to the peak value seen in the control simulation (*solid line*) and remains there. Even in the case of fast adaptation described above, Ca^{2+} release does not terminate under the conditions of SR clamp (not shown). These simulations suggest that JSR depletion is essential for termination of Ca^{2+} release from the SR. Upon first glance, it might seem that in these simulations Ca^{2+} release termination by the SR depletion is due to a lack of releasable Ca^{2+} in the JSR. This, however, is not the case. Instead, it is the reduction of the gradient for Ca^{2+} between the JSR and the subspace that terminates release. Once this gradient diminishes, there is not enough Ca^{2+} entering the subspace to trigger and sustain regenerative release. To demonstrate this point, $[Ca^{2+}]_{JSR}$ is clamped to half its resting value (0.588 mM; Fig. 7, *long dashed line*). With this partial SR clamp, the AP had longer duration with an elevated plateau compared with the control (not shown). There is no regenerative release from the SR, as indicated by the small $[Ca^{2+}]_i$ transient (Fig. 7 *A*) and the tiny RyR open fraction (Fig. 7 *C*). Even a large (10 μM) step in $[Ca^{2+}]_{ss}$ at stimulation does not initiate CICR. However, if P_{O_1} is increased transiently to 0.7 (and P_{C_1} decreased accordingly) at stimulation, CICR does occur, depleting the $[Ca^{2+}]_{JSR}$ to levels similar to those seen during the control AP. Thus the Ca^{2+} release flux from the SR is insufficient to maintain CICR, even though there is still releasable Ca^{2+} in the JSR. During a control AP, the level of $[Ca^{2+}]_{JSR}$ falls below the value of the partial SR clamp (Fig. 7 *B*), indicating that there is still releasable Ca^{2+} in the store. From these sets of simulations, it is clear that JSR Ca^{2+} depletion terminates CICR, whereas RyR adaptation has only a small effect on Ca^{2+} release. Thus, during the course of an AP, Ca^{2+} release from the SR is terminated by depletion of the JSR, whereas RyR adaptation only modulates Ca^{2+} release. Furthermore, the amount of Ca^{2+} released via RyR during an AP can be assessed to show that the SR as a whole is not depleting most of its Ca^{2+} content. In the model the SR is subdivided into two functional compartments, the JSR (Fig. 7 *B*, *solid line*) and NSR (Fig. 7 *B*, *dashed line*). Calculations show that the amount of Ca^{2+} that leaves the JSR is ~28% of the total SR Ca^{2+} content with 1.8 mM external Ca^{2+}. This compares well with the value of 35% by Bassani and co-workers (Bassani et al., 1995) for an external Ca^{2+} concentration of 2.0 mM measured in ferret ventricular myocytes. According to the trend they observed, a lower external Ca^{2+} will yield a lower fraction released.

Pacing protocols

The results above illustrate model behavior over the relatively short time scale of one AP. However, many phenomena associated with E-C coupling depend on the stimulus interval, and hence evolve over a time course of many APs. These phenomena, known as the interval-force relations, describe the changes in force generation as pacing frequency changes. In most species, when the pacing frequency is increased, the amount of force generated in response to an AP rises to a new steady value after a transient decrease (Bers, 1991). Upon a reduction of pacing frequency to its original value, the force generated returns to its previous steady level after a transient increase. Sample results for the step changes in pacing frequencies generated by the model are shown in Fig. 8. In this protocol, the stimulus frequency is transiently increased from 0.5 Hz to 1.5 Hz and then returned to 0.5 Hz. The pacing at 0.5 Hz is initially maintained for a long period, so that the simulated myocyte is producing a stable output, as shown by the first seven beats in Fig. 8. The amplitude of the AP decreases

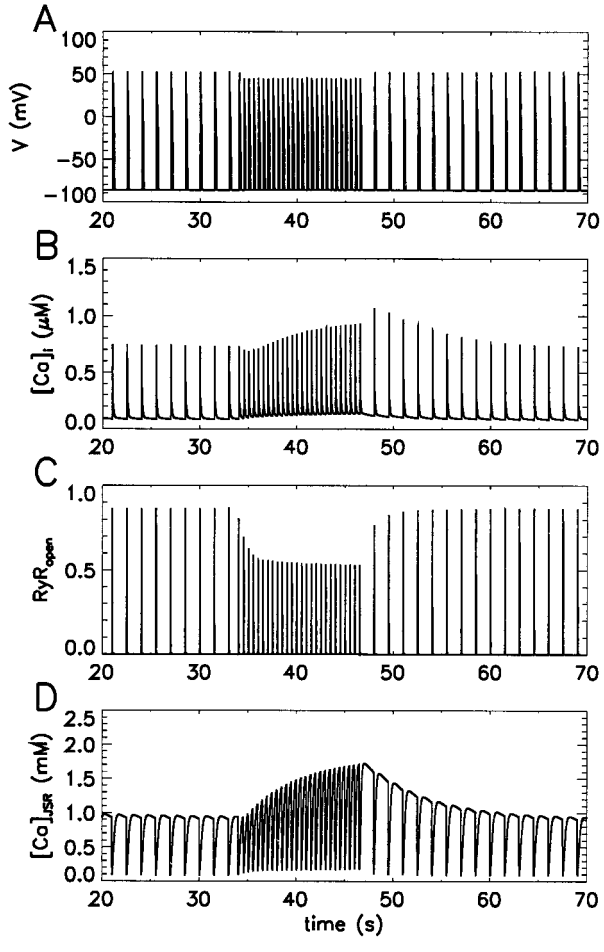

FIGURE 8 The interval-force relation. (*A*) The AP magnitude is slightly smaller during fast pacing. (*B*) After the transition from 0.5 Hz to 1.5 Hz there is a small transient decrease in peak $[Ca^{2+}]_i$ before increasing to a new steady value. After the transition from 1.5 Hz to 0.5 Hz, there is a transient rise in peak amplitude before returning to a lower steady value. (*C*) The peak RyR open fraction is lower during fast pacing. (*D*) The JSR (and NSR) loads with Ca^{2+} during fast pacing. The levels quickly decrease on resumption of a slower pacing rate. The wave train was generated by pacing at 0.5 Hz from 0.0 to 32.0 s, then at 1.5 Hz from 34.0 s to 46.0 s, and back to 0.5 Hz from 48.0 to 70.0 s. In the first 20.0 s (not shown), the wave train approaches the steady wave train shown.

slightly with the increase in stimulation rate (Fig. 8 *A*). The effects of different pacing frequencies upon APs will be described later (Figs. 8–12). When the stimulus frequency is raised to 1.5 Hz, the Ca^{2+} transient decreases initially, but then rises to a new plateau level over the course of the next few beats (Fig. 8 *B*). In contrast, when frequency is decreased, the force increases initially, but then decreases over the course of five beats to a level similar to that originally obtained at 1.5 Hz. Because peak force is a monotonic increasing function of peak Ca^{2+} (Wier and Yue, 1986), one

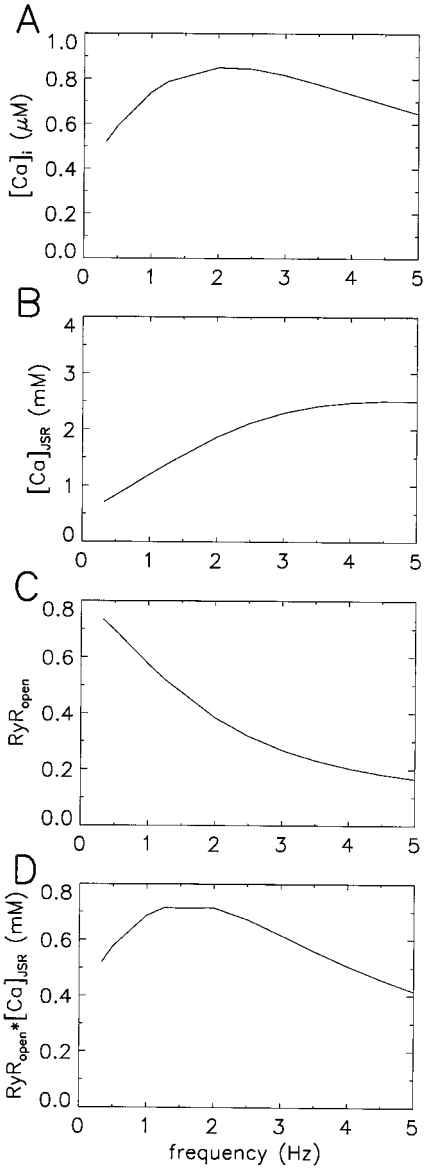

FIGURE 9 The frequency-force relation as indicated by peak systolic $[Ca^{2+}]_i$ is due to the interplay between SR loading and RyR channel open fraction. (*A*) $[Ca^{2+}]_i$ shows the dome-shaped curve seen in typical frequency-force relations. (*B*) The $[Ca^{2+}]_{JSR}$ peak levels (diastolic) increase with increasing pacing frequency. (*C*) The peak RyR open fraction (systolic) decreased with increasing pacing frequency as a result of RyR adaptation. (*D*) The product of $[Ca^{2+}]_{JSR}$ and RyR open fraction yield the dome-shaped curve for peak release flux (J_{rel}), similar to the curve seen in *A*.

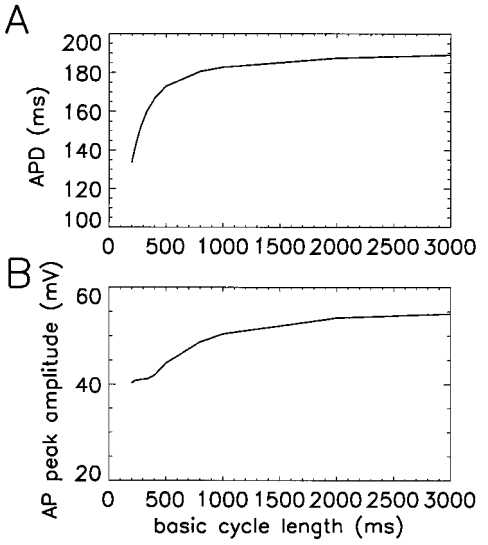

FIGURE 10 (*A*) The action potential duration (APD) increases with increasing basic cycle length (BCL) to a maximum of ~189 ms. (*B*) The AP amplitude increases with increasing BCL to a maximum of ~54.6 mV.

can predict that the model behavior is qualitatively similar to that of force measured in experiments using the same pacing protocol (Bers, 1991).

The changes in peak $[Ca^{2+}]_i$, and hence in peak force, in response to the stimulus frequency changes are quite complex because of both transient and sustained aspects. For example, as frequency is stepped from 0.5 to 1.5 Hz, the force initially decreases, but then recovers to a larger plateau value. With the decrease in frequency, there is a transient increase in $[Ca^{2+}]_i$ transient amplitude before the resumption of a stable wave train. The model suggests a possible mechanism to explain this observed transition behavior. With the increase in frequency, there is initially reduced SR release because the RyRs become refractory with a reduced open probability (Fig. 8 *C*), that is, a larger fraction of RyRs are in the adapted state P_{C_2} and a smaller fraction are in state P_{C_1}, from which Ca^{2+}-induced opening can occur. This rapid decrease in open probability accounts for the early decrease in $[Ca^{2+}]_i$ (and presumably force) seen when pacing frequency is increased. Eventually this effect is compensated for by increased filling of the SR (Fig. 8 *D*). This will increase SR release, even in the face of decreased open fraction of the RyRs, thus explaining the slower increase in $[Ca^{2+}]_i$ (or force with increases in pacing frequency). At higher stimulation rates, the SR loading occurs because the period of time in which Ca^{2+} enters via L-type Ca^{2+} channel and Na^+-Ca^{2+} exchange during a cardiac cycle is increased, i.e., the ratio of systole to diastole increases. In other words, there is an increase in time-averaged Ca^{2+} entry. Similar SR loading has been observed experimentally, and similar mechanisms have been proposed (Bers, 1991). With a decrease in frequency, the RyRs are less refractory and the open fraction increases (Fig. 8 *C*). When coupled with a greater SR loading (Fig. 8 *D*), the

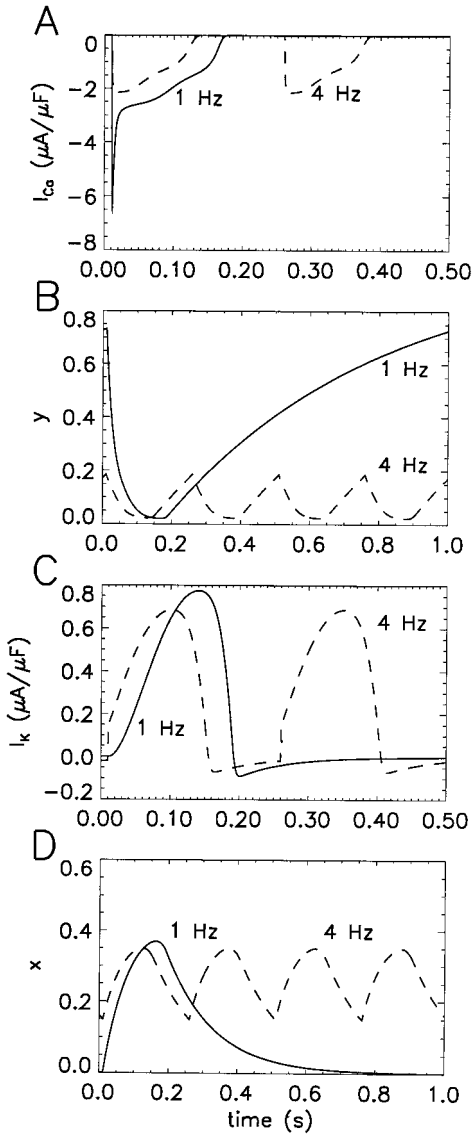

FIGURE 11 Changes in the membrane currents I_K and I_{Ca} lead to changes in APD. (*A*) The magnitude and duration of I_{Ca} at 1.0 Hz (*solid line*) are significantly larger than those at 4.0 Hz (*dashed line*). (*B*) The I_{Ca} inactivation gate y at 1.0-Hz pacing frequency (*solid line*), and the I_{Ca} inactivation gate y at 4.0-Hz pacing frequency (*dashed line*). Note that the value of y at stimulation (peak) is higher in the 1.0-Hz pacing frequency simulation, leading to a larger I_{Ca}. (*C*) At 4.0 Hz (*dashed line*), I_K activates earlier and has a higher resting value than at 1.0 Hz (*solid line*). (*D*) The I_K activation gate x at 1.0-Hz pacing frequency (*solid line*), and the I_K activation gate x at 4.0-Hz pacing frequency (*dashed line*). Note that during diastole the value of x reaches a lower minimum value at 1.0 Hz.

result is a $[Ca^{2+}]_i$ transient (force) of larger amplitude than was seen previously. After a number of beats, the SR loading and release will return to its previous steady-state levels.

In experiments it has been shown that the heart generates different levels of peak force at different pacing frequencies in what is referred to as the frequency-force relation. Studies in guinea pig, human, and cat show a dome-shaped curve with a peak at ~2.0 Hz (Buckley et al., 1972; Hasenfuss et al., 1994; Boyett and Jewell, 1980). A series of simulations were run at various pacing frequencies ranging from 0.33 Hz to 5.0 Hz. Each simulation was run for 30 s to ensure that a stable output was reached. The peak values for the $[Ca^{2+}]_i$ transients for these simulations are plotted by frequency in Fig. 9 *A*. A dome-shaped curve with a peak at 2.0 Hz is obtained. The Ca^{2+} load of the SR increases with increased pacing frequency, consistent with experiment (Bers, 1991), as shown in Fig. 9 *B*. However, because of adaptation, the peak RyR_{open} decreases with increases in frequency (Fig. 9 *C*). J_{rel} depends on the product of the RyR_{open} and the Ca^{2+} gradient, as given in Eq. 4. Because $[Ca^{2+}]_{ss}$ is small compared to $[Ca^{2+}]_{JSR}$, this can be approximated by the product of RyR_{open} and $[Ca^{2+}]_{JSR}$. The result is a dome-shaped curve, as shown in Fig. 9 *D*. Thus the frequency-force relation can be explained as the interplay between adaptation and SR load.

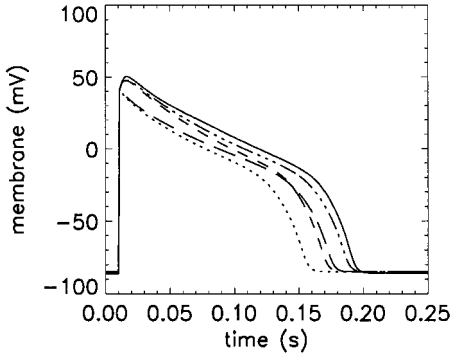

FIGURE 12 Changes in the AP due to modification of the gating variables x and y. The AP traces shown moving from left to right in the descending part of the AP are as follows: AP with 4.0-Hz initial conditions for all variables $x = 0.160706$ and $y = 0.171966$ (*dotted line*); AP with 4.0-Hz initial conditions for all variables, except for y, which is taken from the 1.0-Hz simulation, $x = 0.000928$ and $y = 0.171966$ (*dashed line*); AP with 4.0-Hz initial conditions for all variables, except for x, which is taken from the 1.0-Hz simulation, $x = 0.160706$ and $y = 0.727257$ (*long dashed line*); AP with 4.0-Hz initial conditions for all variables, except for y and x, which are taken from the 1.0-Hz simulation, $x = 0.000928$ and $y = 0.727257$ (*dot-dashed line*); AP with 1.0-Hz initial conditions, $x = 0.000928$ and $y = 0.727257$ (*solid line*). This shows that changes in both I_{Ca} and I_K during rapid pacing result in APD shortening and that changes in I_{Ca} during rapid pacing result in AP amplitude reduction.

Besides changes in the Ca^{2+} transient, there are changes to the AP wave form at different pacing frequencies. For example, it has been observed in dog ventricular cells that the action potential duration (APD) decreases with increasing pacing frequency (Sicouri and Antzelevitch, 1991). This is typically shown as APD increasing with basic cycle length (BCL). Using the set of simulations run to generate Fig. 9, we obtain an increasing curve that plateaus for APD plotted against BCL (Fig. 10 *A*), similar to those observed in experiments. The APD measurements were determined by measuring the time for the membrane potential to exceed −80.0 mV and return to −80.0 mV. Over the range of 200 ms (5.0 Hz) to 3000 ms (0.33 Hz), the APD increases from 133.6 to 189.0 ms. There is also a change in AP amplitude

with BCL (Fig. 10 *B*). As BCL increases from 200 ms to 3000 ms, AP amplitude rises from 40.2 mV to plateau at ~54.6 mV. To understand the changes to the model cell dynamics during increased pacing frequency, we will examine the APs generated at 4.0 Hz and compare them to the AP generated at 1.0 Hz.

Increasing the pacing frequency to 4.0 Hz affects both Ca^{2+} handling and AP shape. The 4.0 Hz $[Ca^{2+}]_i$ transient (0.92 μM) has a larger peak value compared to the 1.0 Hz $[Ca^{2+}]_i$ transient (0.84 μM) shown in Fig. 5 *G*. The diastolic value is also larger (0.19 μM versus 0.10 μM). At the faster pacing rate, $[Ca^{2+}]_{ss}$ has a smaller peak magnitude (17.6 μM) than at 1.0 Hz (22.3 μM). Although the magnitude is lower, more Ca^{2+} is being released because J_{rel} and J_{xfer} are smaller in magnitude but longer in duration. Hence $[Ca^{2+}]_{ss}$ has a longer duration and $[Ca^{2+}]_i$ a larger peak amplitude. Another significant difference at the higher pacing rate is that $[Ca^{2+}]_{JSR}$ and $[Ca^{2+}]_{NSR}$ are considerably higher. At 4.0 Hz the latency for peak $[Ca^{2+}]_i$ is 18.0 ms, which results from the higher diastolic $[Ca^{2+}]_{ss}$ (0.51 μM instead of 0.12 μM). Considering that the Ca^{2+} concentration has increased in all of the intracellular compartments, it is clear that the total amount of Ca^{2+} in the cell has increased. This results from the net increase in Ca^{2+} entry into the cell over a given time interval.

Action potentials generated at 4.0 Hz have a decreased AP duration from 182.8 ms at 1.0 Hz to 146.6 ms at 4.0 Hz. This is accompanied by a decrease in amplitude from 50.4 mV at 1.0 Hz to 40.8 mV at 4.0 Hz. To understand why the AP is modified by varying the pacing frequency, one must consider the membrane currents, in particular, I_{Ca} and I_K. The L-type Ca^{2+} current at 4.0 Hz shown in Fig. 11 *A* (*dashed line*) is smaller in magnitude and of shorter duration than that at 1.0 Hz (*solid line*). The I_{Ca} voltage inactivation gate variable y (Fig. 11 *B*) is the component of L-type Ca^{2+} current that is most altered. At a 1.0-Hz pacing frequency (*solid line*), the diastolic value of y is 0.73 and the systolic value is 0.020. On the other hand, at a 4.0-Hz pacing frequency (*dashed line*), the peak value is 0.17, whereas the minimum value is 0.023. This decrease in peak value accounts for the decrease in L-type Ca^{2+} current. Because I_{Ca} is a depolarizing current, reducing it will decrease APD and AP amplitude. At increased stimulus frequency, I_K has a larger resting value and activates sooner (Fig. 11 *C*), because of changes in its increased open time of the activation gate variable x (Fig. 11 *D*). At 1.0 Hz, x ranges from ~0.0 at systole to 0.37 at diastole. However, at 4.0 Hz, x ranges between 0.16 and 0.35. Because the activation gate does not close completely, there is a greater hyperpolarizing current early in the AP, leading to earlier recovery. Thus the phenomenon of APD dependence on frequency is mainly the result of decreased I_{Ca} and increased I_K.

Recently I_K has been shown to consist of two distinct currents, I_{K_r} and I_{K_s}, and a model of these two distinct currents has been developed (Zeng et al., 1995). These two currents were implemented in our model replacing I_K. I_{K_r} displays faster deactivation kinetics than does I_{K_s}. As a result, even at high pacing rates, I_{K_r} will recover, so that most of the channels are closed, so that it has a similar resting open probability at both 1.0 Hz and 4.0 Hz. Because I_{K_s} has slower deactivation kinetics, it will not recover ompletely at high pacing rates. Hence the I_{K_s} channels achieve higher resting open probabilities at higher pacing frequencies similar to that of x above. Furthermore, the increased influence of I_{K_s} is augmented, because 1.0 Hz has a ~3 times larger magnitude than I_{K_r}. Thus incorporation of separate I_{K_r} and I_{K_s} results in a similar mechanism for APD shortening due to the more dominant behavior of I_{K_s}.

The effects I_{Ca} and I_K on AP duration and amplitude are shown in Fig. 12. The AP traces moving from left to right in the descending part of the AP are generated by varying the initial conditions. The first trace is obtained by pacing at 4.0 Hz. The initial conditions for the gating variables for I_{Ca} and I_K are $x = 0.160706$ and $y = 0.171966$, respectively (*dotted line*). The second trace from the left is obtained by changing the initial value for y to the initial value used in the 1.0-Hz pacing rate simulations to $x = 0.000928$ and $y = 0.171966$ (*dashed line*). Compared to the first trace, the APD is longer and its amplitude is greater. The third trace from the left was obtained by using the initial conditions from the 4.0-Hz simulation (*first trace*) with the value for x changed to the value used in the 1.0 Hz simulation ($x = 0.160706$, $y = 0.727257$; *long dashed line*). In this simulation, the AP is longer than the first and second traces, whereas its amplitude is unchanged from the first. The fourth simulation (*dot-dashed line*) uses the 4.0-Hz initial conditions for all states, except that both x and y are set to the initial 1.0-Hz conditions ($x = 0.000928$, $y = 0.727257$). The amplitude is similar to the second trace, whereas its APD is considerably longer than the first trace. The rightmost trace is obtained from the initial conditions obtained from 1.0-Hz pacing for all state variables ($x = 0.000928$, $y = 0.727257$; *solid line*). Both the APD and amplitude are only a little larger in magnitude than the fourth trace. The initial conditions for x and y are identical for the fourth (*dot-dashed line*) and fifth (*solid line*) traces. All other initial conditions for the fourth trace match those of the 4.0-Hz simulation (*dotted line*). Their similarity when compared to 4.0-Hz simulation suggests that these two factors play a very significant role in APD shortening and AP amplitude reduction. In fact, although I_K causes significant APD shortening, it has little effect on AP amplitude (compare *solid line* to *dashed line*). I_{Ca} exerts a major effect on both APD shortening as well as AP amplitude (compare *long dashed line* with *solid line*), reducing it to the level seen at 4.0-Hz pacing (*dotted line*).

CONCLUDING REMARKS

A new model for Ca^{2+} handling in the ventricular myocyte is presented that incorporates a new formulation for Ca^{2+} handling. This includes 1) SR Ca^{2+} release via RyR channels, which exhibit adaptation; 2) a L-type Ca^{2+} channel

that exhibits mode-switching behavior; 3) a restricted subspace into which the L-type Ca^{2+} channel and RyR empty; 4) Ca^{2+} buffering by calmodulin, calsequestrin, and both high- and low-affinity Ca^{2+} binding sites of troponin; and 5) membrane currents (besides I_{Ca}) from the Luo-Rudy Phase II ventricular cell model. The model has been used to explore adaptation rates from 0.018 ms^{-1} to 0.072 ms^{-1}. These yield time constants of ~56 ms to ~14 ms, which are consistent with the experimental estimates ranging from ~98 ms in dog ventricular SR microsomes (Valdivia et al., 1995) to ~15 ms in rat ventricular SR microsomes (Yasui et al., 1994). The results of the simulations suggest that although RyR adaptation is not necessary for termination of release during a single AP, adaptation is necessary for producing frequency-dependent behavior. As a result, the new Ca^{2+} subsystem appears to produce more realistic E-C coupling behavior than earlier models. For example, the original Luo-Rudy model or recent formulations of the Oxsoft Heart model fail to simulate the force interval or frequency-force relations discussed above (Rice, 1997). This is most likely due to the lack of an explicit model of the RyR with adaptation.

Our model has a small RyR open fraction at rest ($RyR_{open} = 0.0012$), yet upon Ca^{2+} entry, readily undergoes CICR. The major shortcoming of the model is its inability to display a graded Ca^{2+} release response. In addition to the present parameter regime (where adaptation does not terminate release), we also looked at parameter regimes in which adaptation could terminate release. To examine behavior in this regime required changes to some of the model's Ca^{2+} handling parameters, including increasing the RyR adaptation rate in excess of 0.2 ms^{-1}, well above the experimentally determined rate. In this regime the SR did empty to a lesser extent. However, graded release was still not observed. This alternative parameter set is not used because it did not behave well at high pacing frequencies. Stern (Stern, 1992) concluded in a modeling study that to achieve robust graded Ca^{2+} release, one must separate the functional units (cluster of RyRs and L-type Ca^{2+} channels) so that each L-type Ca^{2+} channel and its nearby RyR cluster have their own subspace that is independent of the others. In this case, a graded response will be produced as a result of recruitment of differing numbers of functional units. He reasoned that Ca^{2+} release from RyR is autocatalytic, so that the channel and those immediately surrounding it turn on fully until release is terminated. Hence a common pool model (a model in which all of the release sites empty into the same pool) cannot account for graded release. Being a common pool model, our model also fails to give graded release, even with the enhancements of RyR adaptation. Therefore, we conclude that adaptation alone cannot produce graded release. Furthermore, our model does suggest a role for adaptation. We clearly show that adaptation modifies Ca^{2+} release at different pacing rates. Such behavior could not be reproduced by the Luo-Rudy Phase II model that has graded release but not adaptation. This suggests that during paced AP generation, RyR adaptation may play a larger role in shaping graded SR Ca^{2+} release.

Ours is not the only model of the restricted subspace between the RyRs and L-type Ca^{2+} channels. Langer and Peskoff (1996) recently developed a spatial model of the diadic cleft (the region between the RyR and L-type Ca^{2+} channel) in which Ca^{2+} levels peaked at 600 μM at the cleft center and 100 μM at the periphery of the cleft. Langer and Peskoff modeled the diadic cleft as a circular region with radius 0.2 μm and height 0.12 nm, which yields a volume of 1.5×10^{-3} μm^3 for each cleft. They assume that 67% of the cleft volume is occupied by feet, and that there are 11 L-type Ca^{2+} channels per cleft. Using the estimate of Isenberg of 5500 L-type Ca^{2+} channels per cardiac myocyte yields 500 clefts per myocyte. Thus their total cleft volume would be 0.25 μm^3. We use the data presented by Isenberg (1995), in which the cleft has dimensions $0.3 \times 0.3 \times 0.012$ μm and four L-type Ca^{2+} channels per cleft. With 5500 channels per cell, we get a subspace volume of 1.485 μm^3. Thus the total cleft or subspace volume used by Langer and Peskoff is six times the volume of our subspace. In addition, we do not model the spatial aspects of the cleft, so our model generates a uniform concentration in our subspace with lower peak Ca^{2+} levels. Scaling for volume, their model would predict a peak $[Ca^{2+}]_{ss}$ of less than 16–100 μM. Therefore, both models are in agreement with their prediction of peak Ca^{2+} levels during SR Ca^{2+} release.

The new model for L-type Ca^{2+} channel produces L-type Ca^{2+} current similar to experiments, not unlike the L-type Ca^{2+} current in the Luo-Rudy Phase II model. There were several reasons why a new formulation was necessary. The Luo-Rudy L-type Ca^{2+} current is inactivated instantaneously by elevation in $[Ca^{2+}]_i$. The new formulation presented here is inactivated by $[Ca^{2+}]_{ss}$ which is higher than $[Ca^{2+}]_i$. Simply changing the affinity of Luo-Rudy Phase L-type Ca^{2+} channel Ca^{2+} inactivation would not suffice, because the time course of their $[Ca^{2+}]_i$ transient is triangular, whereas ours declines much more rapidly, in agreement with experiments. As a result, their Ca^{2+} inactivation occurs late in the AP, which concurs with experiments (Grantham and Cannell, 1996). Using instantaneous Ca^{2+} inactivation with a realistic Ca^{2+} transient would only yield Ca^{2+} inactivation early in the AP. However, with the new formulation, based on mode switching, Ca^{2+} inactivation does not change instantaneously with $[Ca^{2+}]_{ss}$, and can produce an accurate L-type Ca^{2+} current.

In cardiac myocytes, Ca^{2+} is responsible for force generation and is thought to play a role in certain cardiac arrhythmias. In a work in progress we incorporate a model for isometric force generation (Rice et al., manuscript in preparation) into our model. We then study the effects of various pacing protocols on force generation. Early after depolarizations (EADs) might be responsible for certain arrhythmias. Our model can help explore the cellular basis of EADs and serve as a basis of network models to understand whether EADs lead to cardiac arrhythmias.

APPENDIX

1. Ionic currents (Luo and Rudy)

Differential equations

$$\frac{dV}{dt} = I_{Na} + I_{Ca} + I_K + I_{K_1} + I_{K_p} + I_{NaCa} + I_{NaK} + I_{ns(Ca)} + I_{p(Ca)} + I_{Ca,K} + I_{Ca,b} + I_{Na,b} \quad (39)$$

$$\frac{dm}{dt} = \alpha_m(1 - m) - \beta_m m \quad (40)$$

$$\frac{dh}{dt} = \alpha_h(1 - h) - \beta_h h \quad (41)$$

$$\frac{dj}{dt} = \alpha_j(1 - j) - \beta_j j \quad (42)$$

$$\frac{dx}{dt} = \alpha_x(1 - x) - \beta_x x \quad (43)$$

$$\frac{d[Na^+]_i}{dt} = -(I_{Na} + I_{Na,b} + I_{ns,Na} + 3I_{NaCa} + 3I_{NaK})\frac{A_{cap}}{V_{myo}F} \quad (44)$$

$$\frac{d[K^+]_i}{dt} = -(I_K + I_{K_1} + I_{Kp} + I_{ns,K} - 2I_{NaK})\frac{A_{cap}}{V_{myo}F} \quad (45)$$

$$\frac{d[HTRPNCa]}{dt} = k^+_{htrpn}[Ca^{2+}]_i([HTRPN]_{tot} - [HTRPNCa]) - k^-_{htrpn}[HTRPNCa] \quad (46)$$

$$\frac{d[LTRPNCa]}{dt} = k^+_{ltrpn}[Ca^{2+}]_i([LTRPN]_{tot} - [LTRPNCa]) - k^-_{ltrpn}[LTRPNCa] \quad (47)$$

Fast Na^+ current

$$I_{Na} = \bar{G}_{Na} m^3 h j (V - E_{Na}) \quad (48)$$

$$E_{Na} = \frac{RT}{F}\ln\left(\frac{[Na^+]_o}{[Na^+]_i}\right) \quad (49)$$

$$\alpha_m = 0.32\frac{V + 47.13}{1 - e^{-0.1(V+47.13)}} \quad (50)$$

$$\beta_m = 0.08e^{-V/11} \quad (51)$$

For $v \geq -40$ mV,

$$\alpha_h = 0.0 \quad (52)$$

$$\alpha_j = 0.0 \quad (53)$$

$$\beta_h = \frac{1}{0.13(1 + e^{(V+10.66)/-11.1})} \quad (54)$$

$$\beta_j = 0.3\frac{e^{-2.535\times10^{-7}V}}{1 + e^{-0.1(V+32)}} \quad (55)$$

For $v < -40$ mV,

$$\alpha_h = 0.135e^{(80+V)/-6.8} \quad (56)$$

$$\alpha_j = (-127140e^{0.2444V} - 3.474 \times 10^{-5}e^{-0.04391V})\frac{V + 37.78}{1 + e^{0.311(V+79.23)}} \quad (57)$$

$$\beta_h = 3.56e^{0.079V} + 3.1 \times 10^5 e^{0.35V} \quad (58)$$

$$\beta_j = 0.1212\frac{e^{-0.01052V}}{1 + e^{-0.1378(V+40.14)}} \quad (59)$$

Time-dependent K^+ current I_K

$$I_K = \bar{G}_K X_i X^2 (V - E_K) \quad (60)$$

$$E_K = \frac{RT}{F}\ln\left(\frac{[K^+]_o + P_{Na,K}[Na^+]_o}{[K^+]_i + P_{Na,K}[Na^+]_i}\right) \quad (61)$$

$$\bar{G}_K = 0.1128\sqrt{\frac{[K^+]_o}{5.4}} \quad (62)$$

$$X_i = \frac{1}{1 + e^{(V-56.26)/32.1}} \quad (63)$$

$$\alpha_X = 7.19 \times 10^{-5}\frac{V + 30}{1 - e^{-0.148(V+30)}} \quad (64)$$

$$\beta_X = 1.31 \times 10^{-4}\frac{V + 30}{-1 + e^{0.0687(V+30)}} \quad (65)$$

Time-independent K^+ current I_{K_1}

$$I_{K_1} = \bar{G}_{K_1} K_{1\infty}(V - E_{K_1}) \quad (66)$$

$$E_{K_1} = \frac{RT}{F}\ln\left(\frac{[K^+]_o}{[K^+]_i}\right) \quad (67)$$

$$\bar{G}_{K_1} = 0.75\sqrt{\frac{[K^+]_o}{5.4}} \quad (68)$$

$$K_{1\infty} = \frac{\alpha_{K_1}}{\alpha_{K_1} + \beta_{K_1}} \quad (69)$$

$$\alpha_{K_1} = \frac{1.02}{1 + e^{0.2385(V - E_{K_1} - 59.215)}} \quad (70)$$

$$\beta_{K_1} = \frac{0.4912e^{0.08032(V-E_{K_1}+5.476)} + e^{0.06175(V-E_{K_1}-594.31)}}{1 + e^{-0.5143(V-E_{K_1}+4.753)}} \quad (71)$$

Plateau K^+ current I_{K_p}

$$I_{Kp} = \bar{G}_{Kp}K_p(V - E_{Kp}) \quad (72)$$

$$E_{Kp} = E_{K_1} \quad (73)$$

$$K_p = \frac{1}{1 + e^{(7.488-V)/5.98}} \quad (74)$$

Na^{2+}-Ca^{2+} exchanger current I_{NaCa}

$$I_{NaCa} = k_{NaCa}\frac{1}{K_{m,Na}^3 + [Na^+]_o^3}\frac{1}{K_{m,Ca} + [Ca^{2+}]_o}\frac{1}{1 + k_{sat}e^{(\eta-1)VF/RT}} (e^{\eta VF/RT}[Na^+]_i^3[Ca^{2+}]_o - e^{(\eta-1)VF/RT}[Na^+]_o^3[Ca^{2+}]_i) \quad (75)$$

Na^{2+}-K^+ pump

$$I_{NaK} = \bar{I}_{NaK}f_{NaK}\frac{1}{1 + \left(\frac{K_{m,Nai}}{[Na^+]_i}\right)^{1.5}}\frac{[K^+]_o}{[K^+]_o + K_{m,Ko}} \quad (76)$$

$$f_{NaK} = \frac{1}{1 + 0.1245e^{-0.1VF/RT} + 0.0365\sigma e^{-VF/RT}} \quad (77)$$

$$\sigma = \frac{1}{7}(e^{([Na^+]_o/67.3} - 1) \quad (78)$$

Nonspecific Ca^{2+}-activated current $I_{ns(Ca)}$

$$I_{ns(Ca)} = I_{ns,Na} + I_{ns,K} \quad (79)$$

$$I_{ns,Na} = \bar{I}_{ns,Na}\frac{1}{1 + (K_{m,ns(Ca)}/[Ca^{2+}]_i)^3} \quad (80)$$

$$\bar{I}_{ns,Na} = P_{ns(Ca)}\frac{VF^2}{RT}\frac{0.75[Na^+]_ie^{VF/(RT)} - 0.75[Na^+]_o}{e^{VF/(RT)} - 1} \quad (81)$$

$$I_{ns,K} = \bar{I}_{ns,K}\frac{1}{1 + (K_{m,ns(Ca)}/[Ca_{2+}]_i)^3} \quad (82)$$

$$\bar{I}_{ns,K} = P_{ns(Ca)}\frac{VF^2}{RT}\frac{0.75[K^+]_ie^{VF/(RT)} - 0.75[K^+]_o}{e^{VF/(RT)} - 1} \quad (83)$$

Sarcolemmal Ca^{2+} pump current $I_{p(Ca)}$

$$I_{p(Ca)} = \bar{I}_{p(Ca)}\frac{[Ca^{2+}]_i}{K_{m,p(Ca)} + [Ca^{2+}]_i} \quad (84)$$

Ca^{2+} background current $I_{Ca,b}$

$$I_{Ca,b} = \bar{G}_{Ca,b}(V - E_{Ca,N}) \quad (85)$$

$$E_{Ca,N} = \frac{RT}{2F}\ln\left(\frac{[Ca^{2+}]_o}{[Ca^{2+}]_i}\right) \quad (86)$$

Na^+ background current $I_{Na,b}$

$$I_{Na,b} = \bar{G}_{Na,b}(V - E_{Na,N}) \quad (87)$$

$$E_{Na,N} = E_{Na} \quad (88)$$

RyR channel states (Keizer and Levine)

$$\frac{dP_{O_1}}{dt} = -k_a^+[Ca^{2+}]_{SS}^nP_{C_1} + k_a^-P_{O_1} \quad (89)$$

$$\frac{dP_{O_2}}{dt} = k_a^+[Ca^{2+}]_{SS}^nP_{C_1} - k_a^-P_{O_1} - k_b^+[Ca^{2+}]_{SS}^mP_{O_1} + k_b^-P_{O_2} - k_c^+P_{O_1} + k_c^-P_{C_2} \quad (90)$$

$$\frac{dP_{C_1}}{dt} = k_b^+[Ca^{2+}]_{SS}^mP_{O_1} - k_b^-P_{O_2} \quad (91)$$

$$\frac{dP_{C_2}}{dt} = k_c^+P_{O_1} - k_c^-P_{C_2} \quad (92)$$

Tables

TABLE 1 Cell geometry parameters

Parameter	Definition	Value
A_{cap}	Capacitive membrane area	1.534×10^{-4} cm^2
V_{myo}	Myoplasmic volume	25.84×10^{-6} μl
V_{JSR}	Junctional SR volume	0.12×10^{-6} μl
V_{NSR}	Network SR volume	2.098×10^{-6} μl
V_{SS}	Subspace volume	1.485×10^{-9} μl

TABLE 2 Standard ionic concentrations

Parameter	Definition	Value (mM)
$[K^+]_o$	Extracellular K^+ concentration	5.4
$[Na^+]_o$	Extracellular Na^{2+} concentration	140.0
$[Ca^+]_o$	Extracellular Ca^{2+} concentration	1.8

TABLE 3 SR parameters

Parameter	Definition	Value
v_1	Maximum RyR channel Ca^{2+} permeability	1.8 s^{-1}
v_2	Ca^{2+} leak rate constant from the NSR	5.80×10^{-5} s^{-1}
v_3	SR Ca^{2+}-ATPase maximum pump rate	1.8 μM s^{-1}
$K_{m,up}$	Half-saturation constant for SR Ca^{2+}-ATPase pump	0.5 μM
τ_{tr}	Time constant for transfer from NSR to JSR	34.48 ms
τ_{xfer}	Time constant for transfer from subspace to myoplasm	3.125 ms
k_a^+	RyR $P_{C_1} - P_{O_1}$ rate constant	0.01215 μM^{-4} ms^{-1}
k_a^-	RyR $P_{O_1} - P_{C_1}$ rate constant	0.1425 ms^{-1}
k_b^+	RyR $P_{O_1} - P_{O_2}$ rate constant	0.00405 μM^{-3} ms^{-1}
k_b^-	RyR $P_{O_2} - P_{O_1}$ rate constant	1.930 ms^{-1}
k_c^+	RyR $P_{O_1} - P_{C_2}$ rate constant	0.018 ms^{-1}
k_c^-	RyR $P_{C_2} - P_{O_1}$ rate constant	0.0008 ms^{-1}
n	RyR Ca^{2+} cooperativity parameter $P_{C_1} - P_{O_1}$	4
m	RyR Ca^{2+} cooperativity parameter $P_{O_1} - P_{O_2}$	3

TABLE 4 L-type Ca^{2+} channel parameters

Parameter	Definition	Value
f	Transition rate into open state	0.3 ms^{-1}
g	Transition rate out of open state	2.0 ms^{-1}
f'	Transition rate into open state for mode Ca	0.0 ms^{-1}
g'	Transition rate out of open state	0.0 ms^{-1}
b_1	Mode transition parameter	2.0
b_2	Mode transition parameter	2.0
ω	Mode transition parameter	0.01 ms^{-1}
$\bar{P}_{Ca}$	L-type Ca^{2+} channel permeability to Ca^{2+}	54.0×10^{-4} cm s^{-1}
$\bar{P}_K$	L-type Ca^{2+} channel permeability to K^+	1.0×10^{-7} cm s^{-1}
$I_{Ca_{half}}$	I_{Ca} level that reduces $\bar{P}_K$ by half	-0.458 μA μF

TABLE 5 Buffering parameters

Parameter	Definition	Value
$[LTRPN]_{tot}$	Total myoplasmic troponin low-affinity site concentration	70.0 μM
$[HTRPN]_{tot}$	Total myoplasmic troponin high-affinity site concentration	140.0 μM
k_{htrpn}^+	Ca^{2+} on rate constant for troponin high-affinity sites	2.0×10^7 μM^{-1} s^{-1}
k_{htrpn}^-	Ca^{2+} off rate constant for troponin high-affinity sites	0.066 s^{-1}
k_{ltrpn}^+	Ca^{2+} on rate constant for troponin low-affinity sites	4.0×10^7 μM^{-1} s^{-1}
k_{ltrpn}^-	Ca^{2+} on rate constant for troponin low-affinity sites	40.0 μM^{-1} s^{-1}
$[CMDN]_{tot}$	Total myoplasmic calmodulin concentration	50.0 μM
$[CSQN]_{tot}$	Total network SR calsequestrin concentration	15.0 mM
K_m^{CMDN}	Ca^{2+} half saturation constant for calmodulin	2.38 μM
K_m^{CSQN}	Ca^{2+} half saturation constant for calsequestrin	0.8 mM

TABLE 6 Membrane current parameters

Parameter	Definition	Value
F	Faraday's constant	96.5 coul $mmol^{-1}$
T	Absolute temperature	310 K
R	Ideal gas constant	8.314 $Jmol^{-1}$ K^{-1}
$\bar{G}_{Na}$	Maximum Na^+ channel conductance	12.8 mS μF^{-1} (16.0)
$P_{Na,K}$	Na^+ permeability of K^+ channel	0.01833
$\bar{G}_{Kp}$	Maximum plateau K^+ channel conductance	0.00828 mS μF^{-1} (0.0183)
k_{NaCa}	Scaling factor of Na^+-Ca^{2+} exchange	5000 μA μF^{-1} (2000)
$K_{m,Na}$	Na^+ half saturation constant for Na^+-Ca^{2+} exchange	87.5 mM
$K_{m,Ca}$	Ca^{2+} half saturation constant for Na^+-Ca^{2+} exchange	1.38 mM
k_{sat}	Na^+-Ca^{2+} exchange saturation factor at very negative potentials	0.1
η	Controls voltage dependence of Na^+-Ca^{2+} exchange	0.35
$\bar{I}_{NaK}$	Maximum Na^+-K^+ pump current	1.3 μA μF^{-1} (1.5)
$K_{m,Nai}$	Na^+ half saturation constant for Na^+-K^+ pump	10.0 mM
$K_{m,Ko}$	K^+ half saturation constant for Na^+-K^+ pump	1.5 mM
$P_{ns(Ca)}$	Nonspecific current channel permeability	0.0 cms^{-1} (1.75×10^{-7})
$K_{m,ns(Ca)}$	Ca^{2+} half saturation constant for nonspecific current	1.2 μM
$\bar{I}_{p(Ca)}$	Maximum sarcolemmal Ca^{2+} pump current	1.15 μA μF^{-1}
$K_{m,p(Ca)}$	Ca^{2+} half saturation constant for sarcolemmal Ca^{2+} pump	0.5 μM
$\bar{G}_{Ca,b}$	Maximum background Ca^{2+} current conductance	0.006032 mS μF^{-1} (0.003016)
$\bar{G}_{Na,b}$	Maximum background Na^+ current conductance	0.00141 mS μF^{-1}

The original Luo-Rudy Phase II parameters are shown in parenthesis.

TABLE 7 Initial conditions

Variable	Definition	Initial value
t	Time	0.00 ms
V	Membrane potential	-86.1638 mV
m	I_{Na} activation gate	3.28302×10^{-02}
h	I_{Na} inactivation gate	0.988354
j	I_{Na} slow inactivation gate	0.992540
x	I_K activation gate	9.28836×10^{-04}
$[Na^+]_i$	Intracellular Na^+ concentration	10.2042 mM
$[K^+]_i$	Intracellular K^+ concentration	143.727 mM
$[Ca^{2+}]_i$	Myoplasmic Ca^{2+} concentration	9.94893×10^{-05} nM
$[Ca^{2+}]_{NSR}$	Network SR Ca^{2+} concentration	1.24891 mM
$[Ca^{2+}]_{ss}$	Subspace SR Ca^{2+} concentration	1.36058×10^{-04} mM
$[Ca^{2+}]_{JSR}$	Junctional SR Ca^{2+} concentration	1.17504 mM
P_{C_1}	Fraction of channels in state P_{C_1}	0.762527
P_{O_1}	Fraction of channels in state P_{O_1}	1.19168×10^{-03}
P_{O_2}	Fraction of channels in state P_{O_2}	6.30613×10^{-09}
P_{C_2}	Fraction of channels in state P_{C_2}	0.236283
C_0	L-type Ca^{2+} channel closed state mode normal	0.997208
C_1	L-type Ca^{2+} channel closed state mode normal	6.38897×10^{-05}
C_2	L-type Ca^{2+} channel closed state mode normal	1.53500×10^{-09}

Variable	Definition	Initial value
C_3	L-type Ca^{2+} channel closed state mode normal	1.63909×10^{-14}
C_4	L-type Ca^{2+} channel closed state mode normal	6.56337×10^{-20}
O	L-type Ca^{2+} channel conducting state mode normal	9.84546×10^{-21}
C_{Ca0}	L-type Ca^{2+} channel closed state mode Ca	2.72826×10^{-03}
C_{Ca1}	L-type Ca^{2+} channel closed state mode Ca	6.99215×10^{-07}
C_{Ca2}	L-type Ca^{2+} channel closed state mode Ca	6.71989×10^{-11}
C_{Ca3}	L-type Ca^{2+} channel closed state mode Ca	2.87031×10^{-15}
C_{Ca4}	L-type Ca^{2+} channel closed state mode Ca	4.59752×10^{-20}
O_{Ca}	L-type Ca^{2+} channel conducting state mode Ca	0.0
y	I_{Ca} inactivation gate	0.998983
[LTRPNCa]	Fraction Ca^{2+} bound low-affinity troponin-binding sites	9.07139×10^{02} mM
[HTRPNCa]	Fraction Ca^{2+} bound high-affinity troponin-binding sites	0.971295 mM

We thank Joel Keizer for early versions of the Keizer-Levine RyR model and David Yue for his invaluable assistance in formulating the L-type Ca^{2+} channel model. We also thank Mark Cannell for providing the AP clamp protocol to test the model.

This work was supported by National Science Foundation grant BIR-9424313 and the Whitaker Foundation Biomedical Engineering Research Grant Program.

REFERENCES

Bassani, J. W. M., W. Yuan, and D. M. Bers. 1995. Fractional SR Ca release is regulated by trigger Ca and SR Ca content in cardiac myocytes. *Am. J. Physiol.* 268:C1313–C1329.

Berlin, J. R., W. M. Bassani, and D. M. Bers. 1994. Intrinsic cytosolic calcium buffering properties of single rat cardiac myocytes. *Biophys. J.* 67:1775–1787.

Bers, D. M. 1991. Excitation-Contraction Coupling and Cardiac Contractile Force, Vol. 122. Kluwer, Boston.

Bers, D. M., and V. M. Stiffel. 1992. The ratio of ryanodine: dihydropyridine receptors (RyR:DHPR) in cardiac and skeletal muscle and implication for E-C coupling. *J. Mol. Cell. Cardiol.* 24:s.82.

Boyett, M. R., and B. R. Jewell. 1980. Analysis of the effects of changes in rate and rhythm upon electrical activity of the heart. *Prog. Biophys. Mol. Biol.* 36:1–52.

Buckley, N. M., Z. J. Penefsky, and R. S. Litwak. 1972. Comparative force-frequency relationships in human and other mammalian ventricular myocardium. *Pflugers Arch.* 332:259–270.

Cannell, M. B., and D. G. Allen. 1984. Model of calcium movements during activation in the sarcomere of frog skeletal muscle. *Biophys. J.* 45:913–925.

Cannell, M. B., H. Cheng, and W. J. Lederer. 1994. Spatial-non-uniformities in $[Ca^{2+}]_i$ during excitation-contraction coupling in cardiac myocytes. *Biophys. J.* 67:1942–1956.

Cheng, H., M. Fill, H. Valdivia, and W. J. Lederer. 1995. Model of Ca^{2+} release channel adaptation. *Science.* 262:807–809.

Cory, R. C., L. J. McCutcheon, M. O'Grady, A. W. Pang, J. D. Greiger, and J. B. O'Brien. 1993. Compensatory down-regulation of myocardial Ca^{2+} channel in SR from dogs with heart failure. *Am. J. Physiol.* 264:H926–H937.

de Leon, M., Y. Wang, L. Jones, E. Perez-Reyes, X. Wei, T. W. Soong, T. P. Snutch, and D. T. Yue. 1995. Essential Ca^{2+}-binding motif for Ca^{2+}-sensitive inactivation of the L-type Ca^{2+} channels. *Science.* 270: 1502–1506.

DiFrancesco, D., and D. Noble. 1985. A model of cardiac electrical activity incorporating ionic pumps and concentration changes. *Philos. Trans. R. Soc. Lond.* 307:353–398.

Dupont, G., J. Pontes, and A. Goldbeter. 1996. Modeling spiral Ca^{2+} waves in single cardiac cells: role of spatial heterogeneity created by the nucleus. *Am. J. Physiol.* 271:C1390–C1399.

Frank, J. S. 1990. Ultrastructure of the unfixed myocardial sarcolemma and cell surface. *In* Calcium and the Heart. Raven Press, New York. 1–12.

Grantham, C. J., and M. B. Cannell. 1996. Ca^{2+} influx during the cardiac action potential in guinea pig ventricular myocytes. *Circ. Res.* 79: 194–200.

Györke, S., and M. Fill. 1993. Ryanodine receptor adaptation: control mechanism of Ca^{2+} induced Ca^{2+} release in heart. *Science.* 260: 807–809.

Hadley, R. W., and W. J. Lederer. 1991. Ca^{2+} and voltage inactivate Ca^{2+} channels in guinea-pig ventricular myocytes through independent mechanisms. *J. Physiol. (Lond.).* 44:257–268.

Hasenfuss, G., H. Reinecke, R. Studer, M. Meyer, B. Pieske, J. Holtz, C. Holubarsch, H. Postival, H. Just, and H. Drexler. 1994. Relation between myocardial function and expression of sarcoplasmic reticulum Ca^{2+}-ATPase in failing and non-failing myocardium. *Circ. Res.* 75:434–442.

Hess, P. 1990. Calcium channels in vertebrate cells. *Annu. Rev. Neurosci.* 13:337–356.

Hess, P., and R. W. Tsien. 1984. Mechanism of ion permeation through calcium channels. *Nature.* 309:453–456.

Hille, B. 1992. Ionic Channels of Excitable Membranes, 2nd Ed. Sinauer Associates, Sunderland, MA.

Imredy, J. P., and D. T. Yue. 1994. Mechanism of Ca^{2+}-sensitive inactivation of L-type Ca^{2+} channels. *Neuron.* 12:1301–1318.

Isenberg, G. 1995. Cardiac excitation-contraction coupling: from global to microscopic models. *In* Physiology and Pathophysiology of the Heart, 3rd Ed. Developments in Cardiovascular Medicine, Vol. 151. Kluwer Academic Publishers, Boston. 289–307.

Jorgensen, A. O., and K. P. Campbell. 1984. Evidence for the presence of calsequestrin in two structurally different regions of myocardial sarcoplasmic reticulum. *J. Cell. Biol.* 98:1597–1602.

Keizer, J., and L. Levine. 1996. Ryanodine receptor adaptation and Ca^{2+}-induced Ca^{2+} release-dependent Ca^{2+} oscillations. *Biophys. J.* 71: 3477–3487.

Kubicek, M., and M. Marek. 1983. Computational Methods in Bifurcation Theory and Dissipative Structures. Springer-Verlag, New York.

Langer, G. A., and A. Peskoff. 1996. Calcium concentration and movement in the diadic cleft space of the cardiac ventricular cell. *Biophys. J.* 70:1169–1182.

Lederer, W. J., E. Niggli, and R. W. Hadley. 1990. Sodium-calcium exchange in excitable cells: fuzzy space. *Science.* 248:283.

Lindblad, D. S., C. R. Murphey, J. W. Clark, and W. R. Giles. 1996. A model of the action potential and underlying membrane currents in a rabbit atrial cell. *Am. J. Physiol.* 271:H166–H1696.

Luo, C. H., and Y. Rudy. 1994a. A dynamic model of the cardiac ventricular action potential. I. simulations of ionic currents and concentration changes. *Circ. Res.* 74:1071–1096.

Luo, C. H., and Y. Rudy. 1994b. A dynamic model of the cardiac ventricular action potential. II. afterdepolarizations, triggered activity, and potentiation. *Circ. Res.* 74:1097–1113.

Lytton, J., M. Westlin, S. E. Burk, G. E. Shull, and D. H. MacLennan. 1992. Functional comparisons between isoforms of the sarcoplasmic or endoplasmic reticulum family of calcium pumps. *J. Biol. Chem.* 267: 14483–14489.

McDonald, T. F., A. Cavalie, W. Trautwein, and D. Pelzer. 1986. Voltage-dependent properties of macroscopic and elementary calcium channel currents in guinea pig ventricular myocytes. *Pflugers Arch.* 406: 437–448.

Noble, D., and G. Bett. 1993. Reconstructing the heart: a challenge for integrative physiology. *Cardiovasc. Res.* 27:1701–1712.

Nordin, C. 1993. Computer model of membrane current and intracellular Ca^{2+} flux in the isolated guinea pig ventricular myocyte. *Am. J. Physiol.* 265:H2117–H2136.

Nordin, C., and Z. Ming. 1995. Computer model of current-induced early after depolarizations in guinea pig ventricular myocytes. *Am. J. Physiol.* 268:H2440–H2459.

Rice, J. J. 1997. Modeling calcium handling, force generation, and length effects in cardiac cells. Ph.D. thesis. Department of Biomedical Engineering, Johns Hopkins University, Baltimore, MD.

Robertson, S. P., J. D. Johnson, and J. D. Potter. 1981. The time course of Ca^{2+} exchange with calmodulin, troponin, parvalbumin, and myosin in response to transient increases is Ca^{2+}. *Biophys. J.* 34:559–569.

Sachs, F., F. Qin, and P. Palade. 1995. Models of Ca^{2+} release channel adaptation. *Science.* 267:2010–2011.

Santana, L. F., H. Cheng, A. M. Gomez, M. B. Cannell, and W. J. Lederer. 1996. Relation between the sarcolemmal Ca^{2+} current and Ca^{2+} sparks and local control theories for cardiac excitation-contraction coupling. *Circ. Res.* 78:166–171.

Schouten, V. J. A., J. K. van Deen, P. de Tombe, and A. A. Verveen. 1987. Force-interval relationship in heart muscle of mammals: a calcium compartment model. *Biophys. J.* 51:13–26.

Shirokov, R., R. Levis, N. Shirokov, and E. Rios. 1993. Ca^{2+}-dependent inactivation of cardiac L-type Ca^{2+} channels does not affect their voltage sensor. *J. Gen. Physiol.* 102:1005–1030.

Sicouri, S., and C. Antzelevitch. 1991. A subpopulation of cells with unique electrophysiological properties in the deep subepicardium of the canine ventricle: the m cell. *Circ. Res.* 68:1729–1741.

Smith, G. D. 1996. Analytical steady-state solution to the rapid buffering approximation near the open Ca^{2+} channel. *Biophys. J.* 71:3064–3072.

Stern, M. D. 1992. Theory of excitation-contraction coupling in cardiac muscle. *Biophys. J.* 63:497–517.

Tang, Y., and H. G. Othmer. 1994. A model of calcium dynamics in cardiac myocytes based on kinetics of ryanodine-sensitive calcium channels. *Biophys. J.* 67:2223–2235.

Valdivia, H. H., J. H. Kaplan, G. C. R. Ellis-Davies, and W. J. Lederer. 1995. Rapid adaptation of cardiac ryanodine receptor: modulation by Mg^{2+} and phosphorylation. *Science.* 267:1997–1999.

Wagner, J., and J. Keizer. 1994. Effects of rapid buffers on Ca^{2+} diffusion and Ca^{2+} oscillations. *Biophys. J.* 67:447–456.

Wier, W. G., and D. T. Yue. 1986. Intracellular calcium transients underlying short-term force-interval relationship in ferret ventricular myocardium. *J. Physiol. (Lond.).* 376:507–530.

Yasui, K., P. Palade, and S. Györke. 1994. Negative control mechanisms with features of adaptation controls Ca^{2+} release in cardiac myocytes. *Biophys. J.* 67:457–460.

Zeng, J., K. R. Laurita, D. S. Rosenbaum, and Y. Rudy. 1995. Two components of the delayed rectifier K^+ current in ventricular myocytes of the guinea pig type. *Circ. Res.* 77:140–152.